



**AFRL-RY-WP-TR-2010-1024**

# **EFFECTS OF MULTIPLE PHOTON SCATTERING IN DECIDUOUS TREE CANOPIES**

**Michael Greiner, Bradley D. Duncan, and Matthew P. Dierking**

**EO Combat ID Branch**

**EO Sensor Technology Division**

**DECEMBER 2009**

**Interim Report**

**Approved for public release; distribution unlimited.**

*See additional restrictions described on inside pages*

**STINFO COPY**

**AIR FORCE RESEARCH LABORATORY  
SENSORS DIRECTORATE  
WRIGHT-PATTERSON AIR FORCE BASE, OH 45433-7320  
AIR FORCE MATERIEL COMMAND  
UNITED STATES AIR FORCE**

## NOTICE AND SIGNATURE PAGE

Using Government drawings, specifications, or other data included in this document for any purpose other than Government procurement does not in any way obligate the U.S. Government. The fact that the Government formulated or supplied the drawings, specifications, or other data does not license the holder or any other person or corporation; or convey any rights or permission to manufacture, use, or sell any patented invention that may relate to them.

This report was cleared for public release by the USAF 88th Air Base Wing (88 ABW) Public Affairs Office (PAO) and is available to the general public, including foreign nationals. Copies may be obtained from the Defense Technical Information Center (DTIC) (<http://www.dtic.mil>).

AFRL-RY-WP-TR-2010-1024 HAS BEEN REVIEWED AND IS APPROVED FOR PUBLICATION IN ACCORDANCE WITH ASSIGNED DISTRIBUTION STATEMENT.

\*//Signature//

LAWRENCE J. BARNES, Project Engineer  
EO Combat ID Branch  
EO Sensor Technology Division

//Signature//

ROBERT J. FELDMANN, Chief  
EO Combat ID Branch  
EO Sensor Technology Division

//Signature//

BRIAN C. FORD, Colonel, USAF  
Chief, EO Sensor Technology Division  
Sensors Directorate

This report is published in the interest of scientific and technical information exchange, and its publication does not constitute the Government's approval or disapproval of its ideas or findings.

\*Disseminated copies will show “//Signature//” stamped or typed above the signature blocks.

REPORT DOCUMENTATION PAGE				Form Approved OMB No. 0704-0188	
<p>The public reporting burden for this collection of information is estimated to average 1 hour per response, including the time for reviewing instructions, searching existing data sources, gathering and maintaining the data needed, and completing and reviewing the collection of information. Send comments regarding this burden estimate or any other aspect of this collection of information, including suggestions for reducing this burden, to Department of Defense, Washington Headquarters Services, Directorate for Information Operations and Reports (0704-0188), 1215 Jefferson Davis Highway, Suite 1204, Arlington, VA 22202-4302. Respondents should be aware that notwithstanding any other provision of law, no person shall be subject to any penalty for failing to comply with a collection of information if it does not display a currently valid OMB control number. <b>PLEASE DO NOT RETURN YOUR FORM TO THE ABOVE ADDRESS.</b></p>					
1. REPORT DATE (DD-MM-YY) December 2009		2. REPORT TYPE Interim		3. DATES COVERED (From - To) 21 October 2007 – 20 December 2009	
4. TITLE AND SUBTITLE EFFECTS OF MULTIPLE PHOTON SCATTERING IN DECIDUOUS TREE CANOPIES				5a. CONTRACT NUMBER In-house	
				5b. GRANT NUMBER	
				5c. PROGRAM ELEMENT NUMBER 62204F	
6. AUTHOR(S) Michael Greiner, Bradley D. Duncan, and Matthew P. Dierking				5d. PROJECT NUMBER 2003	
				5e. TASK NUMBER 11	
				5f. WORK UNIT NUMBER 2003112Y	
7. PERFORMING ORGANIZATION NAME(S) AND ADDRESS(ES) EO Combat ID Branch (AFRL/RYSJ) EO Sensor Technology Division Air Force Research Laboratory, Sensors Directorate Wright-Patterson Air Force Base, OH 45433-7320 Air Force Materiel Command, United States Air Force				8. PERFORMING ORGANIZATION REPORT NUMBER AFRL-RY-WP-TR-2010-1024	
9. SPONSORING/MONITORING AGENCY NAME(S) AND ADDRESS(ES) Air Force Research Laboratory Sensors Directorate Wright-Patterson Air Force Base, OH 45433-7320 Air Force Materiel Command United States Air Force				10. SPONSORING/MONITORING AGENCY ACRONYM(S) AFRL/RYSJ	
				11. SPONSORING/MONITORING AGENCY REPORT NUMBER(S) AFRL-RY-WP-TR-2010-1024	
12. DISTRIBUTION/AVAILABILITY STATEMENT Approved for public release; distribution unlimited.					
13. SUPPLEMENTARY NOTES PAO Case Number: 88ABW-09-4508; Clearance Date: 26 Oct 2009. This report contains color. This report is based on a PhD dissertation generated to fulfill the requirements of the University of Dayton.					
14. ABSTRACT Detecting objects hidden beneath forest canopies has proven to be a difficult task for optical remote sensing systems. Rather than relying upon the existence of gaps between the leaves, our goal was to use the light that is scattered from the leaves to image through dense foliage. We developed a Monte Carlo canopy propagation model to simulate the scattering of light through a maple tree canopy. We measured several forest parameters, including the gap fraction and maximum leaf area density of a real test canopy and applied them to the model. We ran the simulation for 80° illumination and reported on the results in the ground and receiver planes. We then authenticated the validity of the model by illuminating a test forest at an 80° angle, collecting data both on the canopy floor and in a monostatic receiver, and comparing the results to the simulation. Additionally, we examined the accuracy of the model in accounting for seasonal canopy variations and verify the simulation with experimental results. Lastly, we investigated methods for boosting the signal-to-noise ratio (SNR) of detected photons and make SNR calculations for various illumination angles.					
15. SUBJECT TERMS LADAR, foliage penetration, foliage scattering, laser propagation modeling					
16. SECURITY CLASSIFICATION OF:			17. LIMITATION OF ABSTRACT: SAR	18. NUMBER OF PAGES 80	19a. NAME OF RESPONSIBLE PERSON (Monitor) Lawrence J. Barnes 19b. TELEPHONE NUMBER (Include Area Code) N/A
a. REPORT Unclassified	b. ABSTRACT Unclassified	c. THIS PAGE Unclassified			

# Table of Contents

<u>Section</u>	<u>Page</u>
List of Figures.....	iv
List of Tables.....	vi
1. Summary.....	1
2. Introduction .....	3
2.1 Background.....	3
2.2 Leaf Absorption Spectrum.....	3
2.3 Methodology.....	4
3. Methods, Assumptions, and Procedures .....	6
3.1 Bidirectional Scattering Distribution Functions.....	6
3.2 Monte Carlo Simulation.....	9
3.2.1. Random Propagation Distance .....	13
3.2.2. Leaf Scattering Angles.....	17
3.2.3. Ground and Target Scattering Angles .....	19
3.2.4. Test Canopy Parameters.....	19
3.3 Experimental Verification.....	21
4. Results and Discussions.....	24
4.1 Leaf BSDF Measurement Results.....	24
4.1.1. Calculation of Absorption Coefficient .....	24
4.1.2. Modeling Specular Reflection.....	29
4.1.3. Modeling Transmission and Diffuse Reflection.....	32
4.1.4. Leaf Data Interpolation .....	33
4.1.5. Procedure for Constructing the BSDF.....	35
4.2 Monte Carlo Simulation Results .....	36
4.3 Experimental Verification Results .....	39
4.4 Monte Carlo Results at Various Illumination Angles .....	42
4.4.1. SNR Calculations .....	46
4.4.2. Results of Field of View and Range Gate Filtering .....	48
4.4.3. Additional SNR Considerations .....	50
5. Conclusions and Recommendations .....	51
6. References .....	53
Appendix A: Calculation of Probability of a Ballistic Photon.....	55
Appendix B: APD Field of View Characterization .....	59
Appendix C: Test Canopy GPS Waypoints.....	63
Appendix D: Cable Delay and Dispersion.....	65
Appendix E: Selection of Random Value.....	67
List of Acronyms, Abbreviations and Symbols.....	68

## List of Figures

Figure 1 Absorption Spectrum of Fresh Poplar Leaves <sup>13</sup> .....	4
Figure 2 Photograph of the BSDF Measurement Apparatus .....	7
Figure 3 Schematic Diagram of the BSDF Measurement apparatus .....	7
Figure 4 BSDF of (a) a Fresh Common Maple Leaf, and (b) an Appreciably Dried Common Maple Leaf. ....	9
Figure 5 Example Hemispheric Image Captured Looking Upward within a Grove of Sugar Maple Trees .....	9
Figure 6 The Canopy is Illuminated by a Monostatic Ladar System at an Angle $\theta_{INC}$ .....	10
Figure 7 Monte Carlo Algorithm Flow Chart Describing Photon Propagation through a Tree Canopy .....	11
Figure 8 Leaf Orientation Angles (a) are Defined in the (x,y,z) Canopy Coordinate System, while Leaf Scattering Angles (b) are Defined in the Leaf Coordinate System .....	13
Figure 9 Representative Maple Leaf Area Density as a Function of Canopy Height .....	16
Figure 10 Illustration of Region-to-Region Propagation in a Vertically Segmented Tree Canopy .....	17
Figure 11 Example BSDF for a Sugar Maple Leaf Illuminated at an Incidence Zenith Angle of $110^\circ$ .....	18
Figure 12 Mean Gap Fraction as a Function of Zenith Angle for our Nearby Gove of Sugar Maple Trees .....	21
Figure 13 Image of the Test Canopy as Viewed from the Tower .....	22
Figure 14 12x5 Measurement Grid Beneath the Canopy .....	22
Figure 15 Image of the Path Connecting the Entrance Location to Target as Seen from the Entrance Location .....	23
Figure 16 Measured BSDF Data of Common Maple Leaves for Illumination Angles $\theta_I$ of (a) $0^\circ$ (b) $10^\circ$ (c) $20^\circ$ (d) $30^\circ$ (e) $40^\circ$ (f) $50^\circ$ (g) $60^\circ$ (h) $70^\circ$ and (i) $78^\circ$ .....	25
Figure 17 Measured BSDF Data of Cottonwood Leaves for Illumination Angles $\theta_I$ of (a) $0^\circ$ (b) $10^\circ$ (c) $20^\circ$ (d) $30^\circ$ (e) $40^\circ$ (f) $50^\circ$ (g) $60^\circ$ (h) $70^\circ$ and (i) $78^\circ$ .....	26
Figure 18 Comparison of the Sugar Maple Leaf BSDF and Spectralon® BRDF for Normal Illumination .....	27
Figure 19 Absorption Coefficient for Maple Leaves as a Function of Illumination Angle .....	28
Figure 20 Lambertian Fit to the BRDF (left) and BTDF (right) for (a) Normal Illumination and (b) Illumination at $70^\circ$ .....	29
Figure 21 Separation of the Sugar Maple Leaf Diffuse and Specular .....	30
Figure 22 Normalized, Reverse Rayleigh Fits of the Specular Reflection Data for Illumination Angles of (a) $50^\circ$ , (b) $60^\circ$ , (c) $70^\circ$ , and (d) $78^\circ$ .....	31
Figure 23 Fractional Specular Reflection for Maple Leaves as a Function of Incident Angle .....	32
Figure 24 Fitted Sugar Maple Leaf BSDF Curves for Illumination at $70^\circ$ .....	32
Figure 25 Sugar Maple Leaf BRDF Models Created by Adding the Diffuse and Specular Components at (a) $50^\circ$ , (b) $60^\circ$ , (c) $70^\circ$ , and (d) $78^\circ$ Illumination .....	33
Figure 26 Polynomial Fits of the (a) $0^{th}$ , (b) $1^{st}$ , and (c) $2^{nd}$ Order p-Coefficients Describing the BTDF Data for Sugar Maple Leaves. ....	34
Figure 27 Two Dimensional BRDF Surface Fit for Sugar Maple Leaves. ....	36
Figure 28 Two Dimensional BTDF Surface Fit for Sugar Maple Leaves .....	36
Figure 29 Characteristic Temporal Waveform from those Simulated Photons which Strike the Canopy Floor .....	37
Figure 30 Simulated Ground Plane Beam Footprint for an Illumination Angle of $80^\circ$ .....	37
Figure 31 Simulated Beam Footprint Cross Sections, and Best Fit Gaussian Distributions, in the Range (a) and Cross-Range (b) Dimensions .....	38
Figure 32 Spatial Distribution of Simulated RMS Pulse Widths on the Virtual Canopy Floor (in ns) .....	38
Figure 33 Simulated 1-D Temporal PDF Measured in Pupil Plane of the Virtual Detector .....	39
Figure 34 Image of the Avalanche Photo-Diode Setup .....	40
Figure 35 Characteristic Temporal Waveform Measured by an Upwards Looking Avalanche Photodiode Placed on the Canopy Floor .....	40
Figure 36 Measured Ground Plane Beam Footprint for an Illumination Angle of $80^\circ$ .....	41
Figure 37 Measured Beam Footprint Cross-Section Data, and Best Fit Gaussian Curves, in the Range (a) and Cross-Range (b) Dimensions .....	41
Figure 38 Spatial Distribution of Actual RMS Pulse Widths Measured on the Canopy Floor .....	42
Figure 39 Actual 1-D Temporal PDF Measured with a Range Gated Intensified CCD Camera Located in the Tower .....	42

Figure 40 Simulated Beam Footprint on the Ground for $0^\circ$ (a), $30^\circ$ (b), $60^\circ$ (c) and $80^\circ$ (d) Canopy Illumination Angles.....	43
Figure 41 Cross Section of the Simulated Beam Footprint and Best Fit Gaussian Distribution in the Range (a) and Cross- Range (b) Dimensions .....	43
Figure 42 Photon Arrival Time PDF's without Range Gating or Field of View Filtering for $10^\circ$ (a) and $30^\circ$ (b) Canopy Illumination .....	45
Figure 43 Scatter Plot of Photon Arrival Time versus Angle of Arrival onto Detector for $10^\circ$ (a) and $30^\circ$ (b) .....	46
Figure 44 Contour Plot of SNR as a Function of Gate Delay and Half Field of View after Field of View for a Gate Width of $0.1\mu\text{s}$ for $10^\circ$ (a) and $30^\circ$ (b) Canopy Illumination .....	49
Figure 45 Photon Arrival Time PDF's after both Range Gate and Field of View Filtering for $10^\circ$ (a) and $30^\circ$ (b) Canopy Illumination .....	50

## List of Tables

Table 1 Sugar Maple Leaf Reflection, Transmission and Absorption Coefficients as a Function of Illumination Angle .....	28
Table 2 Eastern Cottonwood Leaf Reflection, Transmission and Absorption Coefficients as a Function of Illumination Angle.....	28
Table 3 Sugar Maple leaf BTDF q-Coefficients.....	34
Table 4 Sugar Maple leaf BRDF q-Coefficients.....	34
Table 5 Eastern Cottonwood leaf BTDF q-Coefficients.....	35
Table 6 Eastern Cottonwood leaf BRDF q-Coefficients .....	35
Table 7 Actual Photon Entrance Locations and Simulated Principle Spot Centers .....	44
Table 8 Best Fit Gaussian Beam Widths and RMS Fitting Errors.....	44
Table 9 Signal-to-Noise Ratios, Gate Delays and Widths, and Half Fields of View for Various Canopy Illumination Angles.....	49
Table 10 Signal-to-Noise Ratios, Gate Delays and Widths, and Half Fields of View for Various Canopy Illumination Angles.....	50

# 1. Summary

Detecting objects hidden beneath forest canopies has proven to be a difficult task for optical remote sensing systems. Rather than relying upon the existence of gaps between the leaves, our goal is to use the light that is scattered from the leaves to image through dense foliage. We develop a Monte Carlo canopy propagation model to simulate the scattering of light through a maple tree canopy. We measure several forest parameters, including the gap fraction and maximum leaf area density of a real test canopy and apply them to the model. We run the simulation for  $80^\circ$  illumination and report on the results in the ground and receiver planes. We then authenticate the validity of the model by illuminating a test forest at an  $80^\circ$  angle, collecting data both on the canopy floor and in a monostatic receiver, and comparing the results to the simulation. Additionally, we examine the accuracy of the model in accounting for seasonal canopy variations and verify the simulation with experimental results. Lastly, we investigate methods for boosting the signal-to-noise ratio (SNR) of detected photons and make SNR calculations for various illumination angles.

As predicted by the simulation, we experimentally verified that a large number of photons are down scattered just after entering the canopy, creating a large spot on the ground beneath the entrance location. We then found that a Gaussian distribution fit the range and cross-range cross-sections of the simulated and measured beam footprints with great accuracy. We also found that the standard deviations of the best-fit Gaussian distributions were on the same order in both simulation and experiment. Additionally, we observed that the pulse widths of the waveforms measured on the ground were similar in both shape and magnitude to those predicted by our simulation. Finally, we found that the measured 1-D temporal probability density function (PDF) of photons returning to the receiver closely matched the PDF predicted by the simulation.

We believe that any mismatch between our simulation and experimental results can be attributed to two factors. First, in the experiment there was a slight misalignment between the trajectory of the initial beam axis and the path cleared in the tree grove, which resulted in a small angular error in the pointing of our beam. Second, and most importantly, the simulation results represent an average over billions of realizations of the canopy while the experiment considers only one real forest realization. Considering these factors, we believe our experimental results correlate very well with our simulation, leading us to conclude that our model is valid.

We then investigated the ability of the canopy propagation model to handles seasonal canopy variations. We first quantified the effects of seasonal changes on two forest parameters: the bidirectional scattering distribution function of individual leaves and the maximum leaf area density of the canopy. Then by applying these parameters to our Monte Carlo canopy propagation model we predicted the effect of seasonal changes on the shape and size of the beam footprint as measured on the ground. We found that as the forest health declines and the leaves fall from the trees the size of the spot on the ground increases. We then experimentally verified the results of the model by illuminating a real forest with a 780nm beam and sampling the beam footprint with an upwards facing avalanche photo-diode (APD) beneath the canopy. The same trend was seen in the experimentally measured data as was predicted by the simulation.

Finally, we used our Monte Carlo canopy propagation model to make predictions about detecting objects through the canopy at several different illumination angles. We have used our Monte Carlo propagation model to simulate the scattering of photons through a dense canopy using several different illumination angles. We found that the scattered beam footprint on the canopy floor is primarily located beneath the entrance location of photons into the canopy for all illumination angles. As a result, illuminating the



canopy above an anticipated target, rather than aiming directly at it, places more photons on the target and immensely increases the signal-to-noise ratio of detectable returning photons.

Additionally, we examined the effects of using a narrow field of view, range gated camera. We found that multiply-scattered photons spend more time in the canopy than do singly-scattered photons, and therefore generally arrive at the virtual receiver plane at a later time. The use of a range gated camera allows us to look past the initial return of backscattered noise photons, increasing the signal-to-noise ratio. Multiple canopy scattering also causes spatial and angular dispersion of photons throughout the canopy. Thus, photons arriving at later times most likely also arrive at larger angles which allows many noise photons to be filtered using a narrow field of view camera.

We found that by illuminating directly above the desired target and using a narrow field of view, range gated camera we found that we can boost the signal-to-noise ratio on the order of 15dB. While our results are specific to the exact geometry and canopy architecture used in this simulation, we have demonstrated in principle that we may boost the signal-to-noise ratio of detected multiply scattered photons using a narrow field of view, range gated camera, ultimately providing the possibility of imaging obscured targets embedded within a dense forest canopy at low illumination angles.

## 2. Introduction

### *2.1 Background*

An on-going problem for the military is finding and identifying objects concealed by foliage or camouflage. Forest canopies are a natural barrier to air or satellite detection using both optical and traditional radar techniques. The traditional approach to imaging objects hidden by foliage relies on synthetic aperture radar (SAR) to penetrate through the leaves.<sup>1,2,3</sup> Because the wavelength is typically on the order of several meters, the light passes through the vegetation with minimal attenuation and therefore, this technique has proven to be successful at detecting targets. However, also because the wavelength is on the order of several meters, the resolution is limited and a clear high definition image cannot be formed. Thus, in the interest of achieving high-fidelity target identification and minimizing false alarms, researchers have been exploring the advantages of active laser imaging since the early 1980s.<sup>4,5</sup>

Current optical foliage penetration methods depend heavily upon looking through gaps between the leaves and branches.<sup>1</sup> For example, as an airborne sensor is flown over a forested area, small pieces of a target under the canopy may be sequentially imaged and later pieced together to form a composite image.<sup>6,7</sup> Unfortunately, the gap fraction quickly drops to zero as the foliage density and/or zenith angle increases, leaving very few opportunities to exploit gaps in the canopy.<sup>8</sup> Rather than relying upon the existence of gaps between the leaves, our goal is to use the light that is scattered from the leaves to image through dense foliage.

### *2.2 Leaf Absorption Spectrum*

At optical wavelengths, absorption occurs within leaves at specific wavelengths due to chlorophyll, water, and other leaf materials.<sup>9</sup> Light absorbed by chlorophyll may be converted into energy through photosynthesis.<sup>10</sup> Chlorophyll has high absorption in the visible spectrum, ranging from the blue (around 445 nm) to the red, around 645nm. Leaf water is also a major constituent of fresh leaves, representing around 66% of a leaf's weight.<sup>11</sup> Leaf water absorption has large absorption features in the infrared range, beginning around 1400nm, but close to zero absorptance in the visible or near infrared part of the spectrum.<sup>12</sup> The overall leaf absorption spectrum is shaped by the spectra of chlorophyll and water, as well as its many other components. An example of the absorption spectrum of a fresh poplar leaf can be seen in Figure 1.<sup>13</sup>

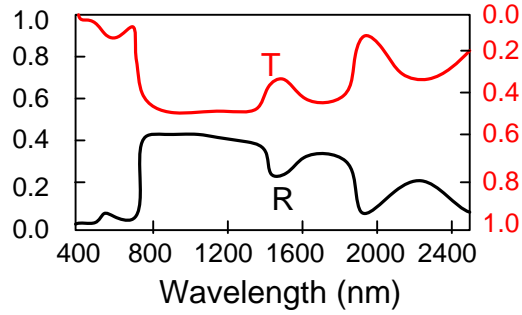


**Figure 1 Absorption Spectrum of Fresh Poplar Leaves**

Light striking any object must be reflected, transmitted, or absorbed. Thus, the figure is broken into three distinct regions: transmittance  $T$ , reflectance  $R$ , and absorptance  $A$ , where the absorptance is determined from  $T$  and  $R$  through the relationship  $A = 1 - R - T$ . For the majority of foliage there is a band of the spectrum, ranging from 800nm to 1400nm, where the absorption of light dips sharply, and transmission and reflection are relatively large and nearly equal. A wavelength found in this low absorption band could potentially be used to penetrate the leaves and, in effect, see through them to reflective objects behind them. These curves are typical of most types of deciduous tree leaves.<sup>14</sup>

### 2.3 Methodology

In Section 2 we discuss several key concepts related to this project. We examine the spectral properties of individual deciduous tree leaves, as well as the bidirectional scattering distribution functions of sugar maple and eastern cottonwood leaves for 1064nm light. We also discuss the forward and reverse transformations of random variables, which we use to select random distances and angles in our Monte Carlo algorithm. Finally, we take a look at the fundamental principles of range gated imaging and define several key terms.

In Section 3 we introduce a canopy propagation model which will allow us to simulate the propagation and scattering of photons through a forest canopy with one hundred percent foliage obscuration. We describe, in detail, the Monte Carlo algorithm along with the individual probability density functions governing each of the random variables we use in this simulation. We discuss the measurement of several parameters from a nearby tree grove and apply them to our model. By using real forest parameters, we intend to achieve the most accurate and reproducible results. We report the findings of our simulations and investigate the validity of the model by comparing several predicted phenomena to that which we measured by propagating a real beam through the canopy of a local maple tree grove.

In Section 4 we investigate the application of the model to seasonal changes in the canopy. As the water in the leaves is replaced with air the index of refraction lowers and the scattering properties change. We therefore look at the seasonal dependence of the BSDF for individual sugar maple and eastern cottonwood leaves. We also examine the seasonal dependence of the leaf number density within a foliated forest by capturing hemispheric images at a set grid of locations beneath the canopy. We apply the measured canopy parameters to our Monte Carlo model and report on the simulation results. We then illuminate our test canopy with a real beam and perform waveform measurement experiments to validate the accuracy of the model's prediction to seasonal changes.

In Section 5 we examine the possibility of using scattered light for imaging through a healthy, foliated canopy. Under the assumption that the canopy propagation model is valid, we run the simulation for a variety of illumination angles and make predictions on the prospect of imaging. We derive an expression for the signal to noise ratio of the detection process as a function of the number of signal and noise photons collected by the detector. We then examine the effects of using a narrow field of view camera as well as implementing range gated imaging and report on their expected boost in signal to noise ratio. Finally, we present a summary of our work and our key conclusions in Section 6.

### 3. Methods, Assumptions, and Procedures

#### 3.1 Bidirectional Scattering Distribution Functions

The scattering and transmission properties of trees and forests are topics of great interest in the field of optical remote sensing. As leaves dominate the scattering of light within a forest canopy, knowledge of their optical properties is essential in order to model the interaction of photons with the canopy. Optical properties of leaves have been the subject of many studies in recent years. These studies have found applications in several fields, including photobiology, agriculture and remote sensing.<sup>12,15,16</sup>

This section focuses upon the bidirectional scattering distribution function (BSDF) of maple and cottonwood leaves. The BSDF of a surface is the ratio of the scattered radiance to incident irradiance at a given wavelength. The function is dependent upon two directional angles, the angle of illumination and the angle at which light is scattered. The BSDF is typically split into reflected and transmitted components, which are treated separately as the bidirectional reflectance distribution function (BRDF) and the bidirectional transmittance distribution function (BTDF), respectively.

Few studies have been performed on the scattering functions of individual leaves because it has typically been assumed that these functions are simply Lambertian in nature.<sup>17,18</sup> However, measurements have not always supported this assumption. In fact, some studies, including our own, have found a strong specular reflection component accompanying the diffuse Lambertian scattering for higher illumination angles.<sup>19,20</sup>

It has been demonstrated that the wavelength of the illuminating laser dramatically changes the scattering properties of leaves. Figure 1 for example, depicts the reflectance and transmittance spectra of fresh poplar leaves. Although poplar (*Populus canadensis*) is not one of the species investigated in this research, the general trend in its absorption spectrum is typical of all deciduous leaves and is therefore relevant to our work. Figure 1 is broken into three distinct regions: transmittance  $T$ , reflectance  $R$ , and absorptance  $A$ , where the absorptance is determined from  $T$  and  $R$  through the relationship  $A = 1 - R - T$ . Notice that the visible region is characterized by high absorptance. There are also strong absorption peaks in the infrared. However, there is a region in the near-IR, between 800 and 1300 nm, where absorptance is minimized. Selecting a wavelength in this region therefore provides the largest amount of light reflected by and transmitted through the leaves. It will thus be the goal of this research to characterize the BSDFs of two deciduous leaf species in the local Dayton, OH area (i.e., Sugar Maple and Eastern Cottonwood) at a single, near-IR wavelength. Measurement of BSDF data from individual leaves is performed through the use of the goniometric apparatus shown in Figure 2 and depicted schematically in Figure 3. A linearly polarized 1064 nanometer pulsed laser (>6μJ pulse energy) is directed along the axis of a stationary optical rail. A beam splitter is used to send half of the beam to the leaf for scattering and the other half to an energy level detector. The beam directed towards the energy detector is first incident upon a 50% reflective Spectralon® disc. The measured radiant energy reflected from this disc is simply used to monitor pulse-to-pulse energy fluctuations so that data can later be normalized with respect to variations in pulse energy.

Two neutral density (ND) filters, mounted on the rail after the beam splitter, are used to attenuate the power of the laser in order to avoid damaging the transmission and reflection detectors. The ND filters are also tilted slightly in order to avoid direct reflections into the beam path. Notice, though, that any deflection of the beam due to the first filter is counteracted by the second so that the path of the beam remains along the rail axis.

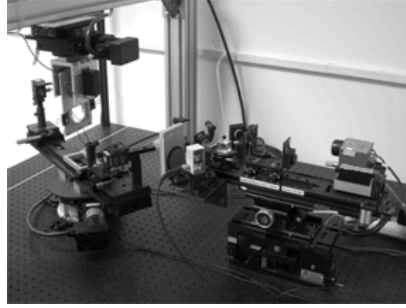


**Figure 2 Photograph of the BSDF Measurement Apparatus**

After attenuation, the laser beam is directed onto the leaf, which is mounted in a goniometer for measurement. The goniometer has two separate, coaxial rotation stages that are motor driven and independently controlled by a computer which also tracks the leaf's rotational position relative to the beam path. A second optical rail is mounted on one of the rotation stages with reflection and transmission detectors equidistant from the leaf at opposite ends of the rail. The active region of the detectors is small enough to give point measurements and avoid angular averaging of the data. The leaf is mounted above this rail on a second rotation stage which is driven by a separate motor. In this way the illumination angle of the beam on the leaf can be adjusted independently of the observation angles.

Each rotation stage is capable of  $360^\circ$  of rotation, allowing the reflection and transmission to be observed at any angle. The rail rotation angle  $\theta_D$  is considered to be at  $0^\circ$  when the transmission detector is at its leftmost position and would see the beam passing through the leaf with no deflection. The leaf rotation angle  $\theta_I$  is considered to be at  $0^\circ$  when the leaf surface is normal to the incident beam.

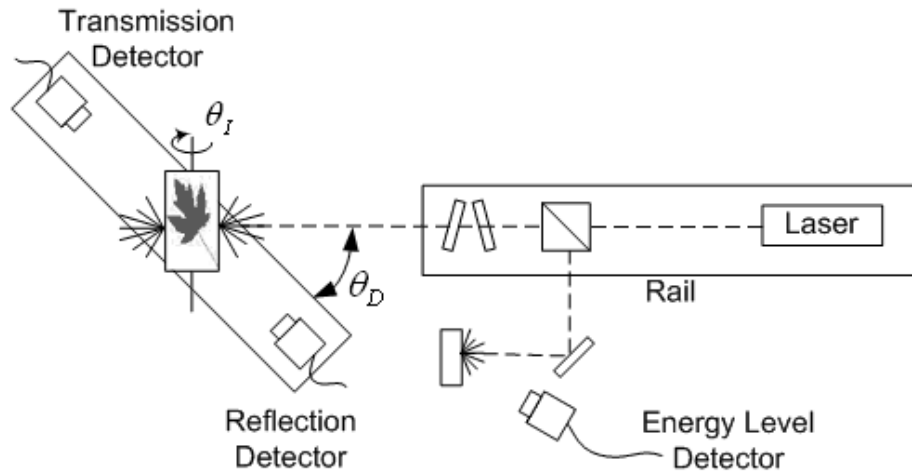


**Figure 3 Schematic Diagram of the BSDF Measurement apparatus**

The motors of both the detector rail and leaf mount are controlled by an automated LabView® program which rotates the detectors and leaf to predetermined angles. At each set of angles the program takes 256 samples from each detector. The samples are then averaged, and a mean value is stored for each detector. The program then moves the leaf and/or detectors to the next set of angles, and the process is repeated until all the desired angle permutations are exhausted. Additionally, the entire procedure is repeated for four different leaves. The four mean values for each detector are then averaged into a single value for every angle permutation. The result is the average of 1024 samples taken from four different leaves. The additional data samples are collected in order to reduce any leaf-to-leaf variance in the final readings.

The diameter of the Gaussian beam is optically set to approximately 1cm to provide a large illumination footprint. This is done for two reasons. First, laser speckle is reduced by increasing the size of the illumination beam. Reducing laser speckle in turn reduces variance in readings made by the detectors. Second, because a leaf's structure is not homogeneous (i.e., leaves have veins and stems, as well as other fine cellular structures running through them), it is important to illuminate a large enough area of the leaf to ensure good spatial averaging.

Speckle reduction and spatial averaging are also enhanced by periodically translating the leaf within the path of the beam. In addition to being mounted on a rotation stage, the leaf is mounted on a vertical translation stage, shown in Figure 2, which is driven at a frequency of approximately 1 Hz. Translating the leaf up and down, coupled with the use of a broad illumination beam, creates a large effective area over which the leaf is sampled. As a result, localized leaf structure has minimal effect on the measurements.

BSDF data was collected from Sugar Maple and Eastern Cottonwood leaves found in the Dayton, Ohio area during the weeks of May 21, 2006 and May 28, 2006. For each leaf species both the bidirectional reflectance (BRDF) and transmittance (BTDF) distribution functions were measured for incident angles of 0, 10, 20, 30, 40, 50, 60, 70, and 78°. Illumination angles higher than 78° were not used because the projected beam waist becomes larger than the physical width of the leaf as it rotates to higher angles. The scan of a single illumination angle then involves taking measurements of the scattered radiance at many detector angles about the leaf surface. We collected data at detector angles spanning a range from -85° to +85° about the leaf surface normal, in increments of 5°.

Because scattering properties change as leaves dry out, scan durations must be kept short.<sup>9</sup> Preliminary experiments showed a strong correlation between the freshness of a leaf and its scattering characteristics. For example, Figure 4 shows the BSDF of a (a) fresh Sugar Maple leaf illuminated with normally incident light, and (b) the same leaf left out to dry overnight. In these figures, light incident from the left (illustrated by the arrow) illuminates a leaf (bold line) at normal incidence. The resulting transmission profile (right hand lobes) and reflection profile (left hand lobes) are plotted in polar coordinates. There are appreciable effects due to leaf drying, as can be seen in the difference in the size of the reflection and transmission lobes between the two plots. In this case, as water in the leaf is replaced with air we observed that the reflectance of leaves increases while the transmittance decreases. Notice that the shape of the two lobes remains relatively constant, though the area encompassed by each changes appreciably.

Because of the effect of leaf drying on the scattering profile, it is necessary to ensure that the leaves remain fresh during the entire measurement procedure. In order to combat the effects of leaf drying, a single leaf was used to scan only three illumination angles before it was replaced with a new, fresh leaf. As the scan of a single illumination angle takes approximately 25 minutes, limiting the use of a single leaf to less than 90 minutes proved short enough that drying effects were not noticeable in any leaves, or our final data.

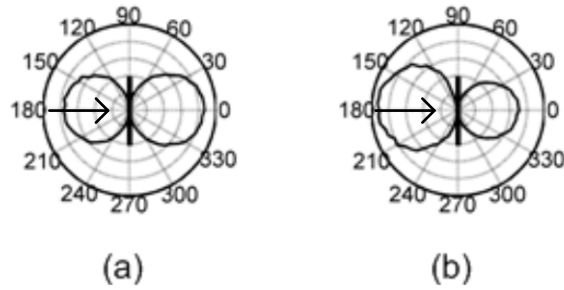


**Figure 4 BSDF of (a) a Fresh Common Maple Leaf, and (b) an Appreciably Dried Common Maple Leaf.**

### ***3.2 Monte Carlo Simulation***

Detecting objects beneath forest canopies is a difficult task for optical remote sensing systems. Current foliage penetration methods depend heavily upon the ability to look through gaps between the leaves and branches.<sup>1</sup> For example, as an airborne sensor is flown over a forested area, small pieces of a target under the canopy may be sequentially imaged and later pieced together to form a composite image.<sup>21,22</sup> Unfortunately, as shown in Figure 24, the gap fraction quickly drops to zero as the foliage density and/or zenith angle increases, leaving very few opportunities to exploit gaps in the canopy.<sup>23</sup> Developing the capability to look directly through leaves while not relying on the existence of gaps will greatly aid in the imaging of objects beneath the canopy.

Imaging from scattered photons presents new and unique challenges. The scattering distributions of individual leaves have been studied extensively, but understanding what happens to light as it is scattered through a random collection of leaves is a more complex problem.<sup>13,24</sup> In particular, after propagating through a canopy a light beam will experience spatial, angular, and temporal dispersion. The distribution of photons exiting the canopy will then be physically wider, de-collimated, and temporally dispersed from the incident beam.<sup>25</sup>

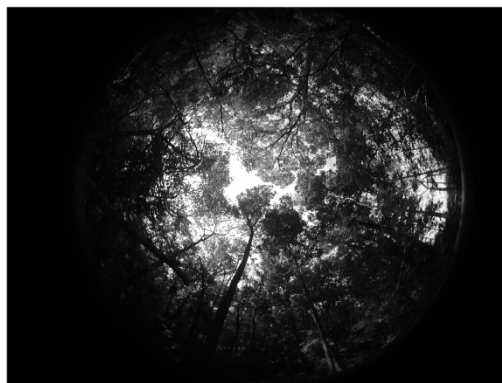


**Figure 5 Example Hemispheric Image Captured Looking Upward within a Grove of Sugar Maple Trees**



The propagation of light through a forest canopy was modeled by means of an extensive Monte Carlo simulation in which multiple scattering events within the canopy are treated as a sequence of interactions between a single photon and a discrete scatterer. Simplification lies in the fact that the end result does not come through looking at the canopy as a whole, but rather by considering each photon individually and each interaction sequentially. The advantage of using Monte Carlo methods is that multiple scattering events can be calculated without complex analysis, as only single variable scattering probability density functions are required.

We use our Monte Carlo algorithm to track the propagation of photons through a simulated canopy which we have modeled as an elliptically cylindrical collection of leaves that are randomly, but not uniformly, distributed. As shown in Figure 25, photons are launched at an illumination angle of  $\theta_{INC}$  from an elevated monostatic direct detection ladar system and are aimed at an assumed primary target located on the ground at the geometric center of the canopy. We have also assumed a secondary ground target beneath the location where photons first enter the canopy, as preliminary simulations showed a large spot on the ground at this location due to initial down-scattering. Both virtual targets are 10m in diameter and are tilted so that their surface normals are pointed back toward the receiver.

The algorithm used is based on the cloud propagation model presented by E. Bucher and is depicted in the flow chart provided in Figure 26.<sup>25</sup> According to our model, a single incident photon enters the canopy and travels a random distance before it experiences its first scattering interaction. On this initial propagation the photon cannot stray from its trajectory and therefore may only encounter a leaf or the primary target at which it is initially aimed. However, there are typically four possible options after random photon propagation: (i) leaf interaction, (ii) target interaction, (iii) ground interaction, or (iv) canopy departure.

If the photon remains within the bounds of the canopy after its initial propagation event, then it must have struck a leaf, and either absorption or scattering will occur. We determine whether or not the photon is absorbed by selecting a value of a random variable uniformly distributed between 0 and 1. If the random value is smaller than the leaf absorption coefficient, then the photon is absorbed and we launch a new photon into the canopy. Otherwise, the photon is scattered from the leaf, in which case we select random leaf orientation angles ( $\theta_L$  and  $\phi_L$ ) and random leaf scattering angles ( $\theta_S$  and  $\phi_S$ ).

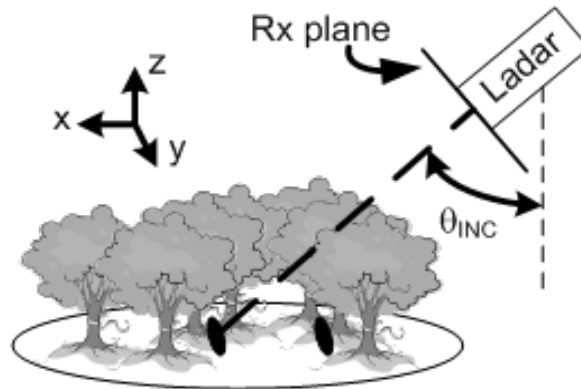


**Figure 6 The Canopy is Illuminated by a Monostatic Ladar System at an Angle  $\theta_{INC}$**

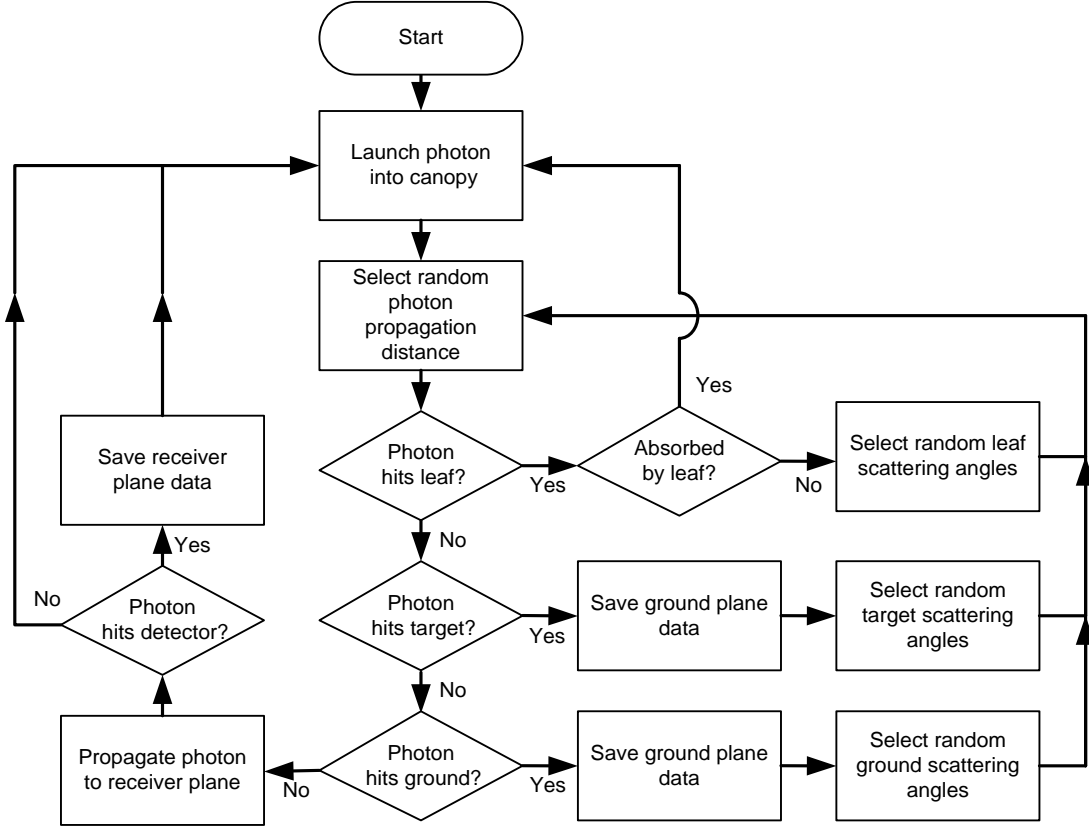


**Figure 7 Monte Carlo Algorithm Flow Chart Describing Photon Propagation through a Tree Canopy**

As shown in Figure 27 (a), the leaf orientation angles ( $\theta_L$  and  $\phi_L$ ) are defined in the canopy coordinate system, where  $\theta_L$  is the zenith angle made between the z-axis and the leaf normal vector  $\hat{n}$ , and  $\phi_L$  is the azimuth angle between the x-axis and the projection of the leaf normal vector onto the x-y plane. The canopy coordinate system is in turn defined so that the origin is located on the ground at the center of the primary target, where the positive x-axis is parallel to the ground and points directly away from the transmitter, the z-axis points straight up, and the y-axis is defined according to the right-hand rule. As shown in Figure 27 (b), the leaf scattering angles ( $\theta_s$  and  $\phi_s$ ) are then defined in the leaf coordinate system, where  $\theta_s$  is the zenith angle made between the leaf surface normal and the scattered photon's unit propagation vector  $\hat{s}$ , and  $\phi_s$  is the azimuth angle made between the projections of  $\hat{s}$  and the photon's unit propagation vector  $\hat{p}$  as it is incident upon the leaf surface.

The photon propagation angles ( $\theta$  and  $\phi$ ), defined in the canopy coordinate system as shown in Figure 27 (a), are then determined using a simple matrix transformation. In particular, after scattering, the scalar components of the unit vector describing the propagation direction  $\hat{s}$  can be expressed in terms of the leaf coordinate system as

$$\begin{bmatrix} x_s \\ y_s \\ z_s \end{bmatrix} = \begin{bmatrix} \sin \theta_s \cos \phi_s \\ \sin \theta_s \sin \phi_s \\ \cos \theta_s \end{bmatrix} \quad (1)$$

This vector must then be transformed into the canopy coordinate system by applying rotation angles  $\phi_L$  and  $\theta_L$  about the z- and y-axes, respectively, according to

$$\begin{bmatrix} x \\ y \\ z \end{bmatrix} = \begin{bmatrix} \cos \theta_L \cos \phi_L & -\sin \phi_L & \sin \theta_L \cos \phi_L \\ \cos \theta_L \sin \phi_L & \cos \phi_L & \sin \theta_L \sin \phi_L \\ -\sin \theta_L & 0 & \cos \theta_L \end{bmatrix} \begin{bmatrix} \sin \theta_s \cos \phi_s \\ \sin \theta_s \sin \phi_s \\ \cos \theta_s \end{bmatrix} \quad (2)$$

From Eq. (3.2) the desired photon propagation angles can then be determined:

$$\theta = \tan^{-1} \left( \frac{\sqrt{x^2 + y^2}}{z} \right) \quad \text{and} \quad \phi = \tan^{-1} \left( \frac{y}{x} \right) \quad (3)$$

Next, if the photon reaches the ground plane, its location is compared to the locations of the two targets. If the photon strikes either of the targets, both of which are assumed to have unit reflectance, we save the spatial, temporal and angular ground plane data and select random target scattering angles ( $\theta_T$  and  $\phi_T$ ). The target scattering angles are then defined in a target coordinate system analogous to the leaf coordinate system, in the sense that the zenith and azimuth angles are determined by the normal vector of the target. Also, by substituting ( $\theta_T$  and  $\phi_T$ ) for ( $\theta_s$  and  $\phi_s$ ), the same matrix transformation described by Eqns. (1)-(3) can be applied to determine the new photon propagation angles in the canopy coordinate system.

If, however, the photon reaches the ground plane but does not interact with a target, it must have struck the ground, which we also assume to have unit reflectance. In this case we save the spatial, temporal, and angular ground plane data and select random ground scattering angles ( $\theta_G$  and  $\phi_G$ ). Note that the ground scattering angles are defined in the canopy coordinate system and therefore describe the new photon propagation angles without further transformation.

Finally, if the random propagation distance places the photon outside the bounds of the canopy we propagate the photon back to the receiver plane. To match our experimental conditions, the receiver plane in our model was assumed to be located 45 m above the ground at a range of 255 m (for 80° illumination) and tilted such that its surface normal is directed toward the primary target at the center of the canopy. If a photon hits the receiver plane within a 25 cm diameter pupil centered on the monostatic transmit/receive ladar axis and within a 45° field of view, then we save the spatial, temporal, and angular receiver plane data and launch a new photon. Otherwise the photon is considered undetected, we do not save any data and then we launch a new photon. In our model, photons that exit the canopy traveling nominally away from the receiver plane will arrive at the detector in the negative time domain. These photons are also discarded as undetected.

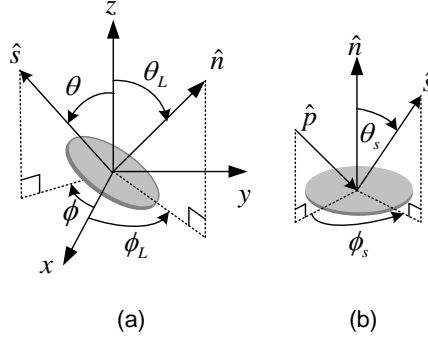


**Figure 8 Leaf Orientation Angles (a) are Defined in the (x,y,z) Canopy Coordinate System, while Leaf Scattering Angles (b) are Defined in the Leaf Coordinate System**

Each photon can travel any distance in any direction according to a number of random variables which must be examined at every step. In particular, the canopy is described completely by the probability density functions describing the following random variables: the propagation distance  $d$ ; the probability that the photon is reflected  $R$ , transmitted  $T$ , or absorbed  $A$  by the leaf; the leaf angular orientation angles  $\theta_L$  and  $\phi_L$ ; the leaf scattering angles  $\theta_s$  and  $\phi_s$ ; the ground scattering angles  $\theta_G$  and  $\phi_G$ ; and the target scattering angles  $\theta_T$  and  $\phi_T$ . The probability density functions for each of the random variables will be described in the following sub-sections. For convenience, a simple method for generating specific values of a random variable, given its probability density function, is discussed in the appendices.

### 3.2.1. Random Propagation Distance

For a *homogeneous* medium of constant leaf number density, the distance  $d$  that the photon travels between scattering events is a random variable described by the following exponential probability density function,<sup>25</sup>

$$p_d(d) = \frac{1}{D} \exp\left[-\frac{d}{D}\right] \quad (4)$$

where the parameter  $D$  is the mean free path, or average distance traveled by the photon between interactions. The mean free path  $D(z, \theta)$  is in turn inversely proportional to the product of the mean projected leaf area  $\overline{A_p}(\theta)$  in the direction of photon propagation and the leaf number density  $N(z)$  of the canopy in the region surrounding the photon. In particular,

$$D(z, \theta) = \frac{1}{\overline{A_p}(\theta) \cdot N(z)} \quad (5)$$

where  $\theta$  is defined in Eq. (3) and  $z$  is the vertical height of the photon within the canopy.<sup>26</sup>

#### 3.2.1.i. Mean Projected Leaf Area

Because leaves mostly face upwards towards the sun, photons traveling at zenith angles  $\theta$  far off the vertical will see less leaf surface area than will photons traveling at smaller angles. Therefore, photons

propagating near the vertical will in general experience a greater number of leaf interactions and have a smaller mean free path than those traveling at greater angles.

To derive an expression for the mean projected area, first suppose that the photon is traveling along the direction  $\hat{s}$  which makes an angle of  $\theta$  with respect to the z-axis, as illustrated in Figure 27(a). Because we will assume that the leaf angular distribution is uniform in the azimuth angle  $\phi$ , we can assume that  $\bar{p}$  lies in the x-z plane and still arrive at a general result. Therefore the photon propagation vector can be expressed as,

$$\bar{p} = \hat{x} \sin \theta + \hat{z} \cos \theta \quad (6)$$

The leaf angle orientation is described by the normal vector  $\bar{n}$ , which can be written as,

$$\bar{n} = \hat{x} \sin \theta_L \cos \phi_L + \hat{y} \sin \theta_L \sin \phi_L + \hat{z} \cos \theta_L, \quad (7)$$

where  $\hat{x}$ ,  $\hat{y}$  and  $\hat{z}$  are Cartesian coordinate system unit vectors. The projected leaf area is then found by means of a vector dot product. Thus, the projected area in the direction of photon propagation can be expressed as,

$$A_p = A_0 \bar{n} \cdot \bar{p} \quad (8)$$

where  $A_0 = \pi d_L^2 / 4$  is the actual leaf area and where we have tacitly assumed circular leaves with a mean effective diameter  $d_L$  of 7.5cm.<sup>27</sup> Inserting the expressions from Eq. (6) and Eq. (7) into Eq. (8), and simplifying, yields the following result

$$A_p = A_0 [\sin \theta_L \cos \phi_L \sin \theta + \cos \phi_L \cos \theta] \quad (9)$$

The last expression is the projected area of a single generalized leaf described by a specific set of leaf orientation angles. To find the mean projected area  $\overline{A_p}(\theta)$ , we must then average this expression over all possible orientation angles. Note, though, that the angles  $\theta_L$  and  $\phi_L$  are governed by their own statistically independent probability density functions  $p_{\theta_L}(\theta_L)$  and  $p_{\phi_L}(\phi_L)$ , respectively, and so are included in the integration as follows:<sup>28</sup>

$$\overline{A_p}(\theta) = \int_{-\infty}^{\infty} \int_{-\infty}^{\infty} A_p(\theta_L, \phi_L : \theta) p_{\theta_L}(\theta_L) p_{\phi_L}(\phi_L) d\phi_L d\theta_L \quad (10)$$

Most often the azimuth angle distribution is assumed to be uniform on the range  $[0, 2\pi)$ , with probability density function (PDF)  $p_{\phi_L}$  then written as, <sup>29,30</sup>

$$p_{\phi_L}(\phi_L) = \frac{1}{2\pi} [u(\phi_L) - u(\phi_L - 2\pi)] \quad (11)$$

where  $u(x - x_0) = \begin{cases} 1 & \text{if } x \geq x_0 \\ 0 & \text{if } x < x_0 \end{cases}$  is the unit step function.<sup>31</sup> The zenith angle PDF  $p_{\Theta_L}$  is, however, commonly considered to be cosinusoidal, being expressed as<sup>27</sup>

$$p_{\Theta_L}(\theta_L) = \left[ u(\theta_L) - u\left(\theta_L - \frac{\pi}{2}\right) \right] \cos \theta_L \quad (12)$$

Notice that this PDF corresponds to leaf normal vectors that are primarily vertical and only rarely horizontal.<sup>32</sup>

The expression for the mean projected area can then be found by inserting Eqns. (9), (11) and (12) into Eq. (10). Solving the integral and simplifying yields the following final expression for the mean projected area,

$$\overline{A_p} = \frac{d_L^2}{4} \left[ \sin \theta + \frac{\pi^2}{4} \cos \theta \right] \quad (13)$$

### 3.2.1.ii. Leaf Number Density

It is commonly accepted that the volume distribution of leaves varies as a function of vertical height  $z$  within the canopy.<sup>33,34</sup> Often the vertical profile of a canopy is described in terms of leaf area density  $L(z)$ , which is a measure of the total leaf area contained within a volume of the canopy. This is a convenient way to characterize the distribution as the leaf area density is readily converted to number density by dividing by the actual mean leaf area.

The expression we used to define the leaf area density function was empirically derived by other researchers and is based on several previously archived forest parameters, including: total canopy height  $h$ , maximum leaf-area density  $L_m$ , and the corresponding canopy height  $z_m$  at which the leaf area density takes on its maximum value.<sup>34</sup> In particular,

$$L(z) = L_m \left( \frac{h - z_m}{h - z} \right)^n \exp \left[ n \left( 1 - \frac{h - z_m}{h - z} \right) \right] \quad (14)$$

where

$$n = \begin{cases} 6 & 0 \leq z \leq z_m \\ 1/2 & z_m \leq z \leq h \end{cases}.$$

As an example, the leaf area density for the canopy we used in our simulation is plotted in Figure 28, where  $h = 18m$ ,  $L_m = 0.6132m^{-1}$ , and  $z_m/h = 0.85$ . Note that the value for  $L_m$  corresponds to our own experimental results, as will be described in Section 4, while the other values were chosen in

accordance with maple tree forest parameters measured by others.<sup>34</sup> The leaf number density function  $N(z)$  is then found by dividing the leaf area density by the actual leaf area,

$$N(z) = \frac{L(z)}{A_0} = \frac{4}{\pi d^2} L_m \left( \frac{h - z_m}{h - z} \right)^n \exp \left[ n \left( 1 - \frac{h - z_m}{h - z} \right) \right] \quad (15)$$

Finally, the expression for the mean free path between scatterers can be determined by inserting Eqns. (13) and (15) into Eq. (5), and simplifying, to yield

$$D(z, \theta) = \frac{\pi}{\left[ \sin \theta + \frac{\pi^2}{4} \cos \theta \right] \cdot L_m \left( \frac{h - z_m}{h - z} \right)^n \exp \left[ n \left( 1 - \frac{h - z_m}{h - z} \right) \right]} \quad (16)$$

### 3.2.1.iii. Selecting a Random Propagation Distance in an Inhomogeneous Medium

Recall that Eq. (4) gives the probability density function for the random propagation distance in a *homogeneous* medium. However, in actuality tree canopies are *inhomogeneous*, as evidenced by the leaf number density changing as a function of canopy height. Our approach to account for this fact was to break the canopy into fifty vertically-stacked horizontal slices, so that the homogeneity of the leaf number density was approximately preserved within each slice. In order to minimize the total number of slices we divided the canopy into non-uniformly spaced regions where the absolute value of the edge-to-edge change in leaf area density was common to each region. As a result, the canopy slices in regions where the leaf area density changes rapidly are thinner than in those regions where it varies slowly. The slices were then treated as separate canopies stacked one on top of the other, and propagation through each slice was treated on a region by region basis.

In any given homogeneous slice of the canopy, a random propagation distance  $d$  is selected using the mean free path of that region. If the propagation distance is less than the distance necessary for the photon to leave the current region, then we assume that there has been a leaf interaction. Otherwise we truncate the propagation at the edge of the current region and begin propagation again in the next region. Note that if the random propagation distance would cause an upward traveling photon to leave the top most region of the canopy we propagate the photon back to the receiver plane and proceed as discussed earlier. Similarly, if the random propagation distance would cause a downward traveling photon to exit the bottom most region, we then terminate propagation at the ground plane and determine whether the photon has struck either the ground or one of the two targets.

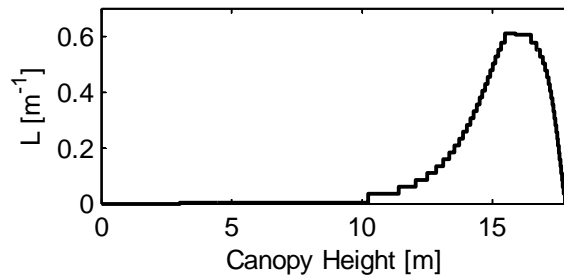


**Figure 9 Representative Maple Leaf Area Density as a Function of Canopy Height**

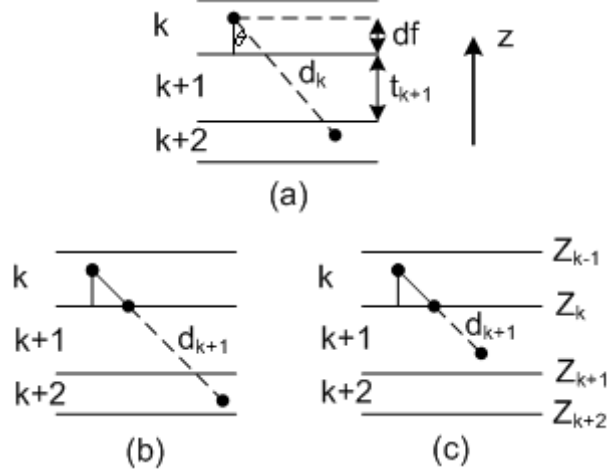


**Figure 10 Illustration of Region-to-Region Propagation in a Vertically Segmented Tree Canopy**

For example, consider a photon propagating at an angle  $\theta$  whose last leaf interaction occurred somewhere in the  $k^{\text{th}}$  region, as shown in Figure 29 (a). The vertical distance between the current location of the photon and the boundary of the next region is  $df$  and the total thickness of  $k^{\text{th}}$  region is given by  $t_k$ . Also, suppose a random value for  $d_k$  is chosen which places the photon outside the  $k^{\text{th}}$  region; that is,  $d_k \cdot \cos \theta > df$ . We then set the total distance traveled in this jump to  $|df / \cos \theta|$  and begin propagating again at the edge of the  $(k+1)^{\text{th}}$  region. Next we use the mean free path for the  $(k+1)^{\text{th}}$  region to select a new propagation distance  $d_{k+1}$ , which is then compared to the thickness of the  $(k+1)^{\text{th}}$  region. If  $d_{k+1} \cdot \cos \theta > t_{k+1}$ , as is illustrated in Figure 29 (b), then the cumulative distance traveled is set to  $|df / \cos \theta| + |t_{k+1} / \cos \theta|$  and the process is restarted at the edge of the  $(k+2)^{\text{th}}$  region. However, if  $d_{k+1} \cdot \cos \theta \leq t_{k+1}$ , as shown in Figure 29 (c), then the photon is assumed to have experienced a leaf interaction in the  $(k+1)^{\text{th}}$  region, the total distance traveled is set to  $|df / \cos \theta| + d_{k+1}$  and the propagation sequence is restarted with new scattering angles.

### 3.2.2. Leaf Scattering Angles

Recall that when a photon interacts with a leaf either absorption or scattering may occur. As previously discussed, we determine whether or not the photon is absorbed by selecting a value of a random variable uniformly distributed between 0 and 1 and comparing it to the absorption coefficient  $A$ . In a similar fashion, when scattering occurs we determine the form of scattering (i.e. either reflection or transmission) by also selecting a value of a random variable uniformly distributed between 0 and 1. In this case, though, if the randomly selected value is between 0 and  $R/(R+T)$ , where  $R$  and  $T$  are the reflection and transmission coefficients of the leaf, respectively, then reflection is assumed to have occurred. Otherwise, the photon is assumed to be transmitted. In our previous work we measured  $R$ ,  $T$ , and  $A$  for healthy sugar maple leaves to be 0.4861, 0.4841, and 0.0298, respectively.



Regardless of the form of scattering, the leaf scattering angles  $\theta_s$  and  $\phi_s$  are generally assumed to be statistically independent with separable PDF's.<sup>35</sup> The scattering azimuth angle is most often taken to be uniformly distributed on the interval  $[0, 2\pi)$ , with its probability density function  $p_{\phi_s}(\phi_s)$  written in the same form as Eq. (11) but with  $\phi_s$  substituted for  $\phi_L$ . We have also previously shown that in reflection the zenith scattering angle can be modeled as the summation of two probability distributions: a lambertian distribution accurately models diffuse scattering from the leaf, while the specular reflection component can be modeled by a Rayleigh distribution. The normalized sum of the two components is then expressed as

$$p_{\Theta_s}(\theta_s) = (1 - F_s) \cos \theta_s + F_s \frac{\left(\frac{\pi}{2} - \theta_s\right)}{\theta_{\text{glint}}^2} \exp\left(-\frac{\left(\frac{\pi}{2} - \theta_s\right)^2}{2\theta_{\text{glint}}^2}\right) \quad (17)$$

where  $F_s$  is the specular reflection fraction and  $\theta_{\text{Inc}}$  is the leaf illumination angle. In the event that transmission takes place the scattering distribution function is assumed to be perfectly Lambertian and the specular reflection fraction is set to zero. Thus, the expression for  $p_{\Theta_s}(\theta_s)$ , above, is valid for both reflection and transmission and integrates to unit area for each individually.

A sample bidirectional scattering distribution function (BSDF) for a sugar maple leaf (*Acer saccharum*), fitted to data measured at an incident zenith angle of  $110^\circ$  is shown in Figure 30. Incident light, shown by the arrow, hits the leaf at  $110^\circ$  (or  $70^\circ$  above the horizontal axis), while the leaf itself is assumed to be oriented vertically so that its surface normal vector  $\hat{n}$  is parallel to the  $0^\circ$  axis. The BSDF lobe on the left is then due to reflection and the lobe on the right is due to transmission. In our previous work we measured BSDF's for both sugar maple and eastern cottonwood (*Populus deltoides*) trees in the local Dayton, Ohio, area and built extensive BSDF models which we have used in our Monte Carlo canopy scattering simulation.

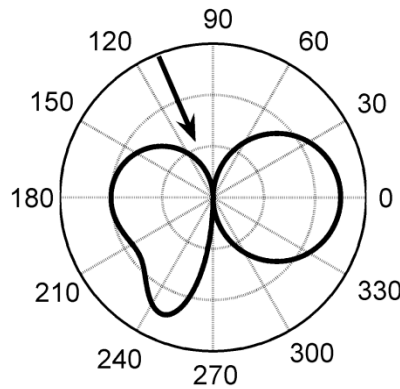


**Figure 11 Example BSDF for a Sugar Maple Leaf Illuminated at an Incidence Zenith Angle of  $110^\circ$**

### 3.2.3. Ground and Target Scattering Angles

When photons reach the ground plane, their location is compared to the locations of the targets. Photons which do not hit either of the targets are assumed to be scattered from the ground. The azimuth and zenith ground scattering angles are again commonly assumed to be statistically independent. In particular, the ground azimuth scattering angle distribution  $p_{\phi_G}(\phi_G)$  is assumed to be uniform over the range  $[0, 2\pi)$  and can be expressed using Eq. (11) after substituting  $\phi_G$  for  $\phi_L$ . The ground zenith scattering angle distribution  $p_{\theta_G}(\theta_G)$  is then governed by a simple Lambertian distribution, nominally describing upward scattering in the positive z-direction, and can be expressed using Eq. (12). after substituting  $\theta_G$  for  $\theta_L$ .<sup>36</sup>

Photons which do hit a target are scattered according to the probability density functions governing the target zenith and azimuth scattering angles. Once again, the two random angles are considered to be statistically independent. As with ground scattering, the target azimuth scattering angle distribution  $p_{\phi_T}(\phi_T)$  is assumed to be uniformly distributed over the interval  $[0, 2\pi)$  and the target zenith scattering angle distribution  $p_{\theta_T}(\theta_T)$  is taken to be Lambertian. The PDFs  $p_{\phi_T}$  and  $p_{\theta_T}$  can then be found by substituting  $\phi_T$  for  $\phi_L$ , and  $\theta_T$  for  $\theta_L$  in Eqns. (11) and (12), respectively.

Recall, however, that both targets are assumed to be tilted so that their surface normals are pointed back in the direction of the receiver. As a result, the target scattering angles must be transformed into the canopy coordinate system as previously discussed. We have done this for two reasons, the first being that in our simulation we increase the probability of receiving photons back from the targets if we nominally tilt them back towards the receiver. And secondly, in real world situations targets will typically have one or more facets that do in fact face back toward the receiver.

### 3.2.4. Test Canopy Parameters

We wished to verify the results of our canopy propagation model with real data collected from within a nearby grove of trees. Therefore, in order to achieve the most reproducible results, we used real parameters measured for this tree grove in our simulation. These include the canopy dimensions, the illumination angle geometry, and the leaf area density.

We illuminated our tree grove using a rudimentary direct detection lidar system located on the 11<sup>th</sup> floor of a tower building at Wright-Patterson Air Force Base, OH. Our lidar system employs a Raman shifted Nd:YAG Coherent Infinity pulsed laser that has been Raman shifted to operate at a wavelength of 1560 nm and produces pulses of ~1 ns duration at a rate of 10 Hz. We frequency doubled the operating wavelength with a LiNbO<sub>3</sub> crystal to 780 nm and added telescoping optics to control the beam diameter down range. The detector is a Princeton Instruments Pi-Max2 intensified CCD camera which is synchronized with the laser for range gating applications. Using a differential GPS unit, we logged the locations of the primary target site and the lidar system located in the tower. We then determined the angle made between the two locations, as well as the distance separating them. We found that the illumination angle was approximately 80° and the horizontal distance between the tower and target was 255 meters.

We then measured the dimensions of the tree grove by walking around the perimeter with a handheld GPS device and periodically logging waypoints around the edge of the tree line. A best fit ellipse was then drawn around the perimeter, with major and minor axis dimensions found to be 358m and 228m,

respectively. Conveniently for us, both the target site and the tower were found to lie along the major axis of this ellipse, allowing us to easily incorporate the actual canopy dimensions into our simulation.

Next we indirectly computed the maximum leaf area density  $L_m$  by first measuring the gap fraction of our test forest at  $80^\circ$ , and by then finding the maximum leaf area density value which would yield the same statistical probability of a photon passing through the canopy without interaction. To measure the gap fraction, we began by capturing sixty hemispheric images, similar to the one shown in Figure 1, from a  $5 \times 12$  point grid of locations under the canopy. We then applied a threshold to the images so that pixels containing leaves and branches were given a value of unity and those without were given a value of zero. Each image was then broken into nine equal area annuli whose bin centers have been mapped to non-uniformly spaced zenith angles.<sup>37</sup> The number of zero valued pixels was counted and then divided by the total number of pixels for each annulus in order to determine the gap fraction as a function of zenith angle. From the 60 individual images, mean gap fraction values were then calculated and plotted at the center of each angular bin, as shown in Figure 31. The interpolated gap fraction value corresponding to 80 degrees was found to be  $11.7\text{e-}3$ .

Gap fraction, typically defined as the percentage of canopy area not covered by leaves, also describes the probability of encountering a gap at a specific zenith angle. That is, if a photon is launched into the simulation at a certain zenith angle, the probability that it will reach the ground without interaction is equal to the gap fraction of the canopy at that angle. Because we modeled propagation through the canopy as a statistical process, we can therefore also calculate the probability of a photon passing unscattered through the simulated canopy as a function of leaf area density.

Recall that the leaf number density varies as a function of canopy height and that for our model we have broken the canopy into 50 regions of constant density. Also recall from Eq. (4) that we model the photon propagation distance between scattering events using a negative exponential probability density function. Therefore, the probability that a photon traveling at zenith angle  $\theta$  experiences a leaf interaction within the  $k^{\text{th}}$  region, (which has mean free path  $D_k$  and upper and lower bounds  $z_{k-1}$  and  $z_k$ , respectively, as shown in Figure 29 (c)) can be found by first integrating this PDF over the region boundaries and then dividing by a normalization factor according to

$$P\{z_{k-1} < z < z_k\} = \frac{\int_{a_{k-1}}^{a_k} \frac{1}{D_k} \exp\left(-\frac{x}{D_k}\right) dx}{\int_{a_{k-1}}^{\infty} \frac{1}{D_k} \exp\left(-\frac{x}{D_k}\right) dx} \quad (18)$$

where  $a_k = z_k / \cos \theta$ . We normalize the above slant path integral in order to account for the fact that if the photon experiences its first leaf interaction within the  $k^{\text{th}}$  region, then it must have already passed through the previous  $k-1$  regions without scattering.

The probability that there will be no leaf interaction within the  $k^{\text{th}}$  region is then found by subtracting Eq. (18) from unity. Correspondingly, the probability of not having an interaction within the entire canopy can be found by evaluating the following product relationship

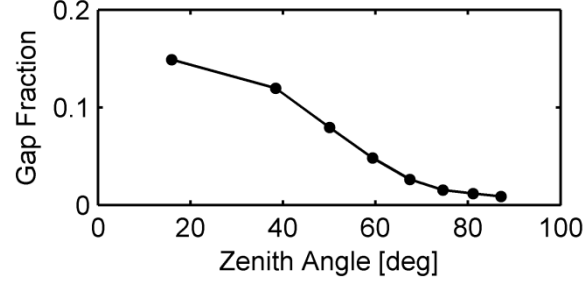


**Figure 12 Mean Gap Fraction as a Function of Zenith Angle for our Nearby Grove of Sugar Maple Trees**

$$P\{\overline{0 < z < h}\} = \prod_{k=1}^K \left[ 1 - \frac{\int_{a_{k-1}}^{a_k} \frac{1}{D_k} \exp\left(-\frac{x}{D_k}\right) dx}{\int_{a_{k-1}}^{\infty} \frac{1}{D_k} \exp\left(-\frac{x}{D_k}\right) dx} \right] \quad (19)$$

We evaluated Eq. (19) for an illumination angle of  $80^\circ$  as we varied the maximum leaf area density. (Recall that the mean free path is a function of  $L_m$ , as given by Eq. (16). The result is shown in Figure 32, and the equation of the best fit curve was found to be

$$P\{\overline{0 < x < h}\} = \exp(-9.0490 \cdot L_m) \quad (20)$$

From this result, we found that a maximum leaf area density of  $L_m = 0.6132 \text{ m}^2/\text{m}^3$  would yield the same probability of an unscattered photon reaching the ground as was determined from the gap fraction measurements. This value is shown by the arrow in Figure 32.

### 3.3 Experimental Verification

In order to validate our model, we collected waveform data from a nearby stand of sugar maple trees during the Summer of 2008. We performed waveform measurements by illuminating the canopy at approximately a  $10^\circ$  angle above the horizon (i.e.,  $80^\circ$  zenith angle) and then sampling the beam footprint on the ground with a grid of avalanche photodiodes (APDs). We sent two beams from the tower, one at 780nm and the other at 1560nm. An image of the test canopy as viewed from the tower is shown in Figure 38, where the beam was aimed at a target placed near the 1C location.



**Figure 13 Image of the Test Canopy as Viewed from the Tower**

We established a reliable trigger signal by placing a 1m diameter, high reflectance spectralon target in a clearing so that it was clearly visible from the tower. Thus we illuminated with the 1560 nm beam. An amplified PIN diode was then stationed 0.5 m in front of the spectralon target and aimed in such a way that the entire target fell within the field of view of the detector. We then relayed the trigger signal through a 500 m co-axial cable to an oscilloscope stationed under the canopy. Keeping the trigger signal at a constant location allowed synchronization of the temporal delays between waveforms measured at different grid point locations.

We then illuminated the tree grove with the 780nm beam which, due to diffraction, had a width of about 10m at the top of the canopy. This beam was directed towards a reflexite (primary) target located near the center of the grove. Note that although our model uses maple leaf BSDF's measured at 1064nm, the scattering functions of these leaves are expected to be very similar under 780nm illumination. We then cleared an 88m path from the primary target toward the tower, with twelve additional 16m paths cleared orthogonal to the beam propagation axis and spaced in uniform 8m intervals. Along these paths we then established five uniformly spaced measurement locations to create a 12x5 measurement grid, as seen in Figure 38. An image of the cleared path beneath the canopy can be seen in Figure 39. We observed that the beam appeared to enter the canopy roughly above the eleventh transverse path, approximately 80m from the primary target.

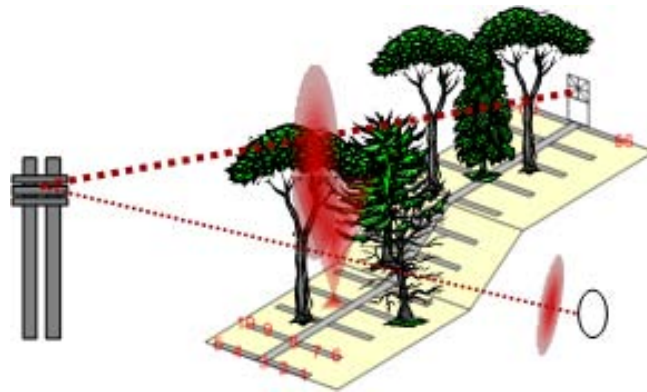


**Figure 14 12x5 Measurement Grid Beneath the Canopy**



**Figure 15 Image of the Path Connecting the Entrance Location to Target as Seen from the Entrance Location**

We then measured the waveforms at each grid location with a Hamamatsu silicon avalanche photodiode, seen in Figure 41, which was mounted on a tripod, aimed directly upwards, and moved from point to point throughout the test. This detector had a field of view of approximately  $45^\circ$ . We then relayed the detected signals to the oscilloscope along with the trigger signal. At each grid point we collected 256 pulses, which we averaged into a single mean waveform and stored for later processing.

## 4. Results and Discussions

### 4.1 Leaf BSDF Measurement Results

Polar plots of the BSDF data collected from maple leaves in the manner described above are provided in Figure 5. The laser beam (depicted by the arrows) was incident upon the leaves at  $\theta_i$  angles of  $0^\circ$ ,  $10^\circ$ ,  $20^\circ$ ,  $30^\circ$ ,  $40^\circ$ ,  $50^\circ$ ,  $60^\circ$ ,  $70^\circ$ , and  $78^\circ$ . A separate sub-figure was made for each illumination angle. Each sub-plot has been normalized such that the sum of the areas of the transmission and reflection lobes is unity. Note that the scaling of the radial axis spans a range from 0 to 0.01 for each subplot, with exception of  $78^\circ$  illumination which goes from 0 to 0.025.

The shape of the BRDF and the BTDF at normal incidence and low illumination angles appear to be largely Lambertian in nature. The radiated energy is located mostly along the leaf surface normal, decreasing cosinusoidally with the rotation of the detector angle. In addition, the shape of the BTDF remains relatively constant regardless of incident angle. However, as the incident angle increases past  $50^\circ$ , the specular component of the reflection increases and the transmission decreases. The glint protrudes only slightly from the diffuse component at  $50^\circ$  and becomes more pronounced as the incidence angle increases. At  $78^\circ$ , the specular component dominates the diffuse reflection. Similar trends are seen in the cottonwood BSDF data shown in Figure 6.

#### 4.1.1. Calculation of Absorption Coefficient

Before investigating BRDF and BTDF features in more detail, it is important to determine the absorption coefficient  $A_L(\theta_i)$  as a function of illumination angle. The method involves measuring the BRDF of a target with a known reflection coefficient  $R_S$  and comparing its area to that of the BRDF and BTDF of a leaf. A 60% reflective Spectralon® disc (i.e.,  $R_S=0.60$  for all  $\theta_i$ ) was used as the standard of measure to which the scattering distributions of the leaves were compared. The normal illumination BRDF of the Spectralon® disc is plotted, for example, along with the maple leaf BSDF for normal illumination in Figure 7. The area of each function is then calculated by integrating over the span of detector angles. That is, the area of the maple leaf BRDF is given by

$$A_R(\theta_i) = \int_{+90}^{+270} r_L(\theta_i, \theta_D) d\theta_D \quad (21)$$

where  $r_L(\theta_i, \theta_D)$  is the BRDF data measured at illumination angle  $\theta_i$  and detector angle  $\theta_D$ . Similarly, the area of the BTDF is given by

$$A_T(\theta_i) = \int_{-90}^{+90} t_L(\theta_i, \theta_D) d\theta_D \quad (22)$$

where  $t_L(\theta_i, \theta_D)$  is the BTDF.

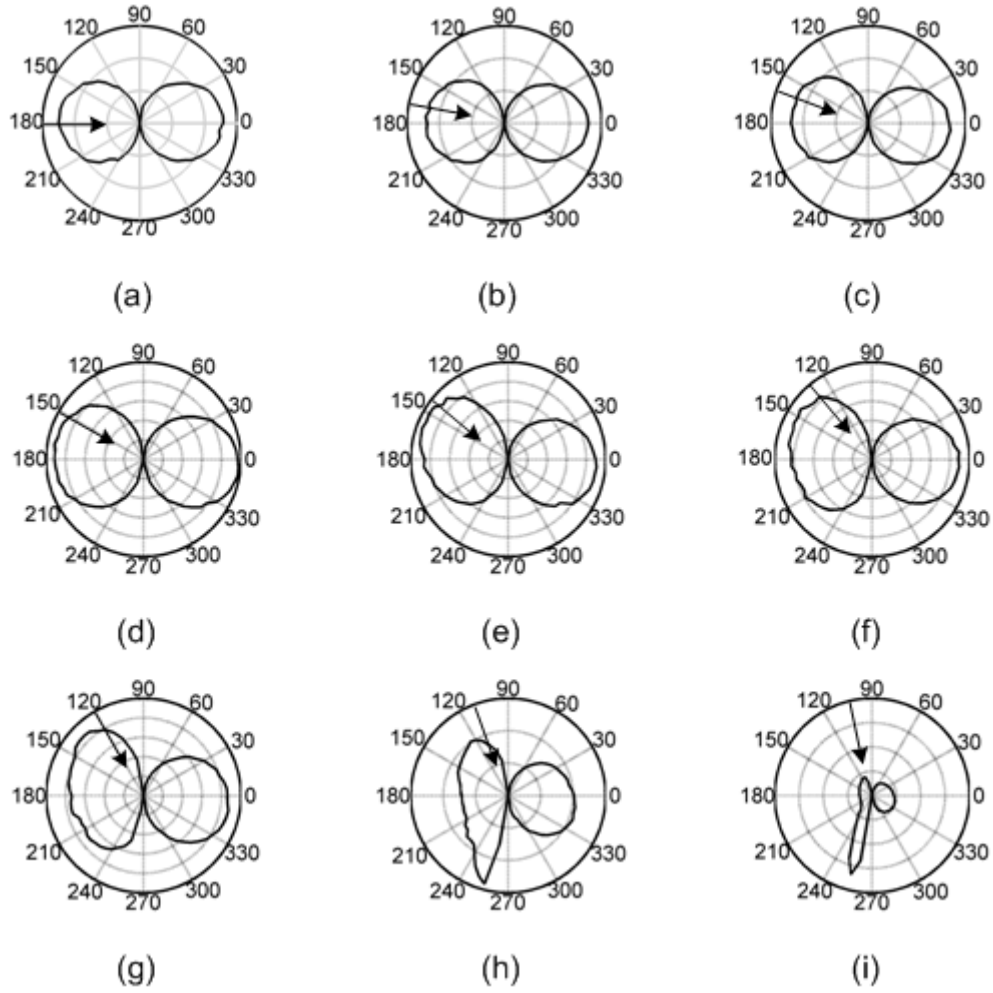


**Figure 16 Measured BSDF Data of Common Maple Leaves for Illumination Angles  $\theta_l$  of (a) 0° (b) 10° (c) 20° (d) 30° (e) 40° (f) 50° (g) 60° (h) 70° and (i) 78°**



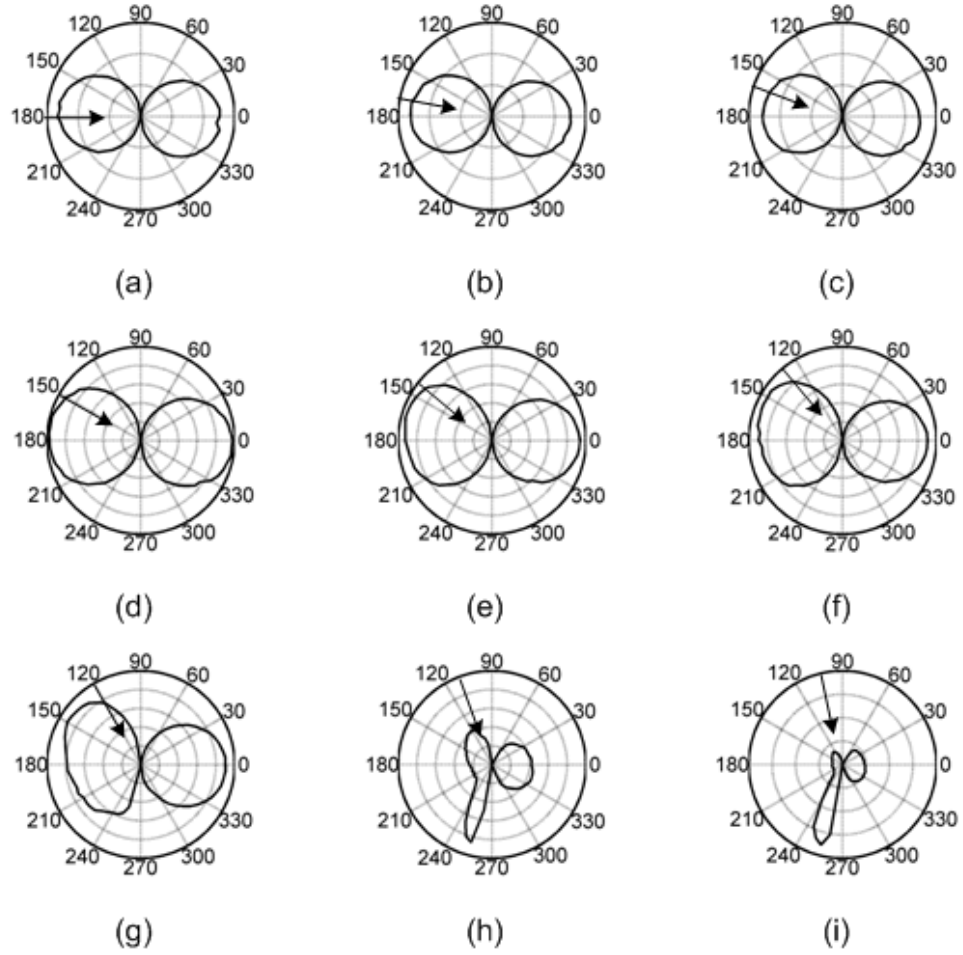


**Figure 17 Measured BSDF Data of Cottonwood Leaves for Illumination Angles  $\theta_l$  of (a)  $0^\circ$  (b)  $10^\circ$  (c)  $20^\circ$  (d)  $30^\circ$  (e)  $40^\circ$  (f)  $50^\circ$  (g)  $60^\circ$  (h)  $70^\circ$  and (i)  $78^\circ$**

The values of the reflection  $R_L(\theta_i)$  and transmission  $T_L(\theta_i)$  coefficients are directly related to the areas under the BRDF and BTDF curves. In particular, the ratio of the reflection coefficients for maple leaves and the Spectralon® disc is equal to the ratio of these areas according to the relationship:

$$\frac{R_L(\theta_i)}{0.60} = \frac{A_R(\theta_i)}{A_S} \quad (23)$$

where  $A_S$  is the area of the spectralon BRDF at normal illumination. A similar expression can be written for the transmission coefficient:

$$\frac{T_L(\theta_i)}{0.60} = \frac{A_T(\theta_i)}{A_S} \quad (24)$$

The absorption coefficient can then be found through the expression

$$A_L(\theta_i) = 1 - R_L(\theta_i) - T_L(\theta_i) \quad (25)$$

Table 1 and Table 2 present values for the reflection, transmission, and absorption coefficients for maple and cottonwood leaves as a function of incident angle. Notice that the transmission coefficients decrease and the reflection coefficients increase with increasing illumination angle. This trend is also seen in the polar plots of the leaf BSDFs in Figures 5 and 6 where the size of the transmission lobe is seen to grow smaller with increasing illumination angle. Another trend evident in Tables 1 and 2 is the growth of absorption with illumination angle.

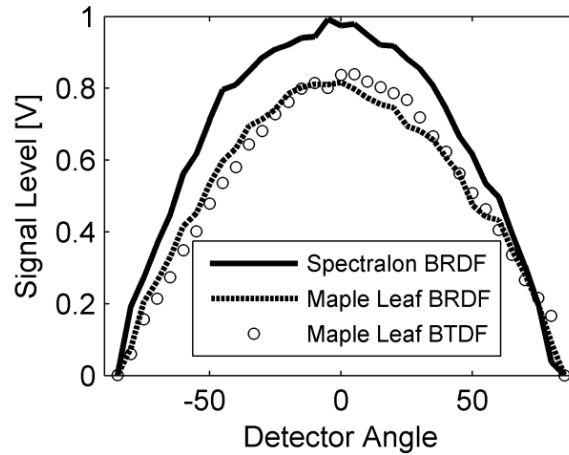


**Figure 18 Comparison of the Sugar Maple Leaf BSDF and Spectralon® BRDF for Normal Illumination**

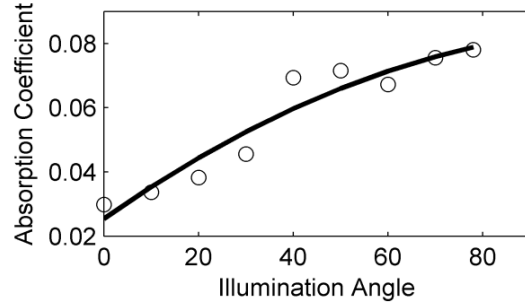


**Figure 19 Absorption Coefficient for Maple Leaves as a Function of Illumination Angle**

The relationship between illumination angle and the absorption coefficient for maple leaves is illustrated in Figure 8. A second order polynomial was fit to the data in order to allow the absorption coefficient for any illumination angle to be calculated. The following two equations, then, describe least square fit regression equations for the absorption coefficients of maple and cottonwood, respectively,

$$A_L(\theta_I) = -4.5156 \times 10^{-6} \times \theta_I^2 + 1.0373 \times 10^{-3} \times \theta_I + 25.415 \times 10^{-3} \quad (26)$$

$$A_L(\theta_I) = 1.1885 \times 10^{-6} \times \theta_I^2 - 67.238 \times 10^{-6} \times \theta_I + 32.7 \times 10^{-3} \quad (27)$$

If desired, the reflection and transmission coefficients can be determined for any illumination angle by integrating the BRDF and BTDF models we will develop in the following sections.

**Table 1 Sugar Maple Leaf Reflection, Transmission and Absorption Coefficients as a Function of Illumination Angle**

$\Phi$	$R_L$	$T_L$	$A_L$
0	0.4861	0.4841	0.0298
10	0.4879	0.4784	0.0337
20	0.4890	0.4727	0.0383
30	0.4884	0.4661	0.0456
40	0.4900	0.4406	0.0694
50	0.4984	0.4300	0.0716
60	0.5000	0.4327	0.0673
70	0.5009	0.4235	0.0756
78	0.5031	0.4188	0.0781

**Table 2 Eastern Cottonwood Leaf Reflection, Transmission and Absorption Coefficients as a Function of Illumination Angle**

$\Phi$	$R_L$	$T_L$	$A_L$
0	0.5414	0.4263	0.0323
10	0.5451	0.4227	0.0322
20	0.5500	0.4178	0.0322
30	0.5519	0.4160	0.0321
40	0.5548	0.4131	0.0321
50	0.5596	0.4084	0.0320
60	0.5457	0.4221	0.0322
70	0.5836	0.3847	0.0317
78	0.5801	0.3834	0.0365

### 4.1.2. Modeling Specular Reflection

In Figure 20 (a), the maple leaf BRDF and BTDF for normally incident light are fitted with a cosine curve normalized to the integrated area of the measured data. The measured data is depicted by the circles, while the fitted curve is given by the solid line. The quality of the fit suggests that both the BRDF and BTDF are accurately modeled by a Lambertian distribution function for normal incidence. Similar results were seen for the other illumination angles less than  $50^\circ$ . However, as the illumination angle increases beyond  $50^\circ$ , other features become apparent. For example, plotted in Figure 20 (b) are the  $70^\circ$  illumination angle BRDF and BTDF data fitted with normalized area cosine curves. While the transmission data remains nearly Lambertian, the reflection data exhibits other features that will be addressed in this section.

Because of the irregularities in the shape of the reflection curves, it is difficult to model the BRDF data with a simple distribution. Also, the specular reflection peak at high incident angles makes it difficult to accurately replicate the curves by simply using high order polynomials. One approach to modeling the BRDF is to separate the specular and diffuse components. Accurate models individually representing the diffuse and specular profiles can then be found separately and later added together to produce the full BRDF model.

Under the assumption that the specular component is negligible for *detector angles* less than  $40^\circ$ , the BRDF can be broken into two regions: one corresponding only to diffuse reflection ( $\theta_d < 40^\circ$ ), and the other containing both specular and diffuse elements ( $\theta_d > 40^\circ$ ). Separation of the two components in the latter region is then performed by fitting a polynomial curve to the known diffuse data and interpolating values within this region. Subtracting the interpolated diffuse data from the overlapping region leaves only the specular reflection component.

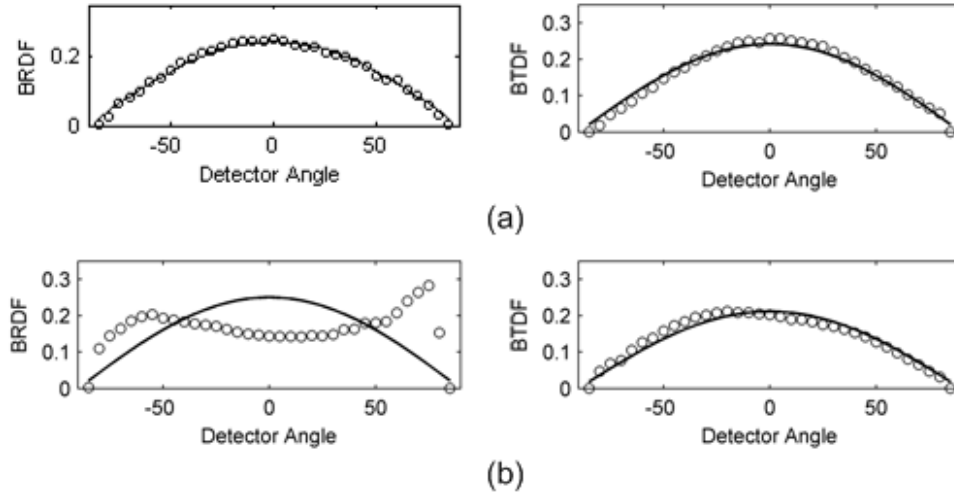


**Figure 20 Lambertian Fit to the BRDF (left) and BTDF (right) for (a) Normal Illumination and (b) Illumination at  $70^\circ$**

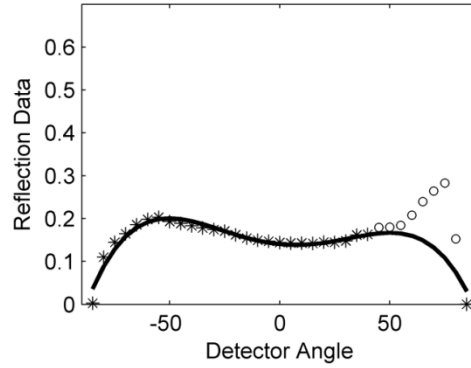


**Figure 21 Separation of the Sugar Maple Leaf Diffuse and Specular Reflection Components for 70° Illumination**

This process is illustrated in Figure 21 for maple leaf BRDF data taken at 70° illumination angle. The non-separated BRDF data is depicted by the stars and circles, which in turn represent the diffuse and overlapping regions, respectively. A fourth order polynomial is fit to the diffuse data and represented by the solid line. The specular reflection component is then found by subtracting the diffuse reflection fit from the measured data. This is shown for the 50, 60, 70, and 78 degree illumination angles in Figure 22.

As also shown in Figure 22, we found that the specular data is best fit with a normalized, reversed Rayleigh distribution of the form,

$$r_s(\theta_D) = F_s(\theta_I) \frac{(90 - \theta_D)}{(90 - \theta_p)^2} \exp \left[ -\frac{(90 - \theta_D)^2}{2(90 - \theta_p)^2} \right] \quad (28)$$

where  $F_s(\theta_I)$  is the fractional specular reflection,  $\theta_D$  is the detector angle, and  $\theta_p$  is the angle at which the function is a maximum. Interestingly, we found that a  $\theta_p$  value of 75° produced the best fit for all incidence angles.

The area of the reversed Rayleigh distribution must be normalized to the fractional area of the specular reflection peak before reconstructing the data with this model. Dividing the area of the specular reflection peak,  $A_{RS}(\theta_I)$ , by the total area of the reflection lobe,  $A_R(\theta_I)$ , for a given incident angle  $\theta_I$  gives the fractional specular reflection according to

$$F_s(\theta_I) = A_{RS}(\theta_I) / A_R(\theta_I) \quad (29)$$

As is seen in Figure 22, the fraction of specular reflection is dependent on the illumination angle. For illumination angles less than 50°, specular reflection is negligible and  $F_s(\theta_I \leq 50^\circ) = 0$ . Moreover, at 90° incidence it is assumed that all reflection is specular, yielding  $F_s(90^\circ) = 1$ . Using these bounds, the fractional specular reflection was fit with a third order polynomial as shown in Figure 23 for maple leaves. The ratio of specular to total reflection for any illumination angle  $\theta_I$  (in degrees) can then be

written empirically as a piecewise continuous function according to the following equations provided for Sugar Maple and Eastern Cottonwood leaves, respectively,

$$F_s = \begin{cases} 0 & , \theta_i < 50 \\ 12.7 \times 10^{-6} \times \theta_i^3 - 1.7 \times 10^{-3} \times \theta_i^2 + 77.2 \times 10^{-3} \times \theta_i - 1.19 & , \theta_i \geq 50 \end{cases} \quad (30)$$

$$F_s = \begin{cases} 0 & , \theta_i < 50 \\ -1.65 \times 10^{-6} \times \theta_i^3 + 922 \times 10^{-6} \times \theta_i^2 - 79.2 \times 10^{-3} \times \theta_i + 1.89 & , \theta_i \geq 50 \end{cases} \quad (31)$$

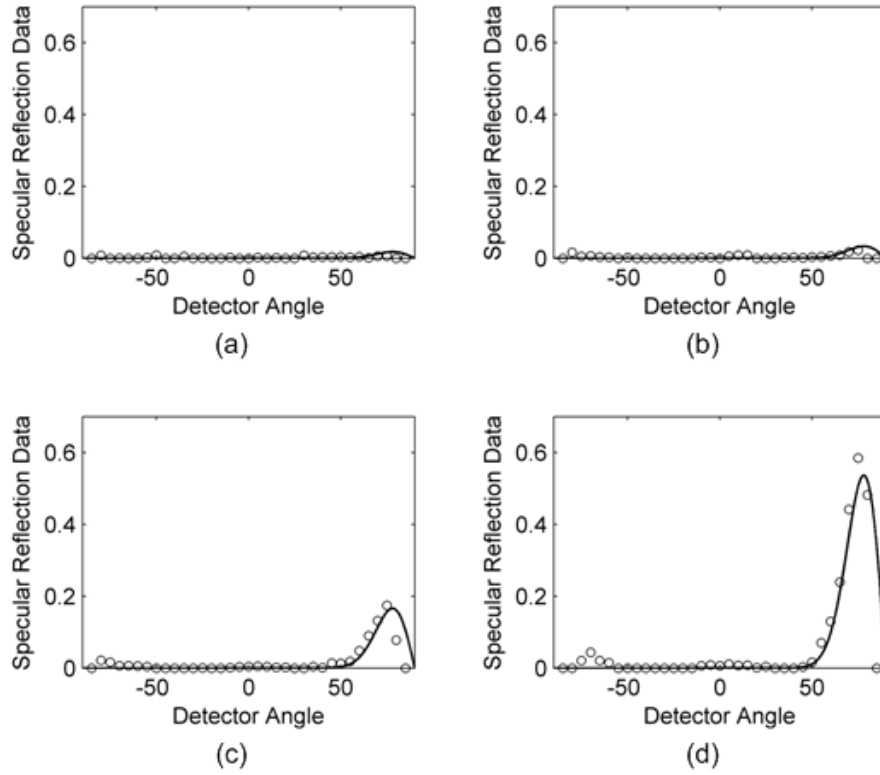


**Figure 22 Normalized, Reverse Rayleigh Fits of the Specular Reflection Data for Illumination Angles of (a) 50°, (b) 60°, (c) 70°, and (d) 78°.**

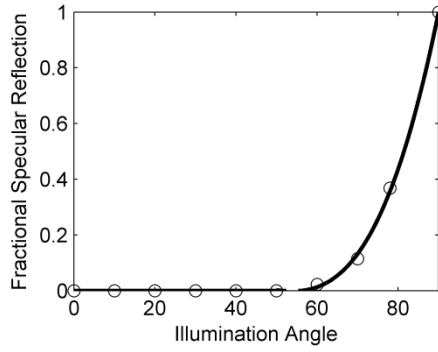


**Figure 23 Fractional Specular Reflection for Maple Leaves as a Function of Incident Angle**

#### 4.1.3. Modeling Transmission and Diffuse Reflection

Both the diffuse reflection and the transmission distribution functions are simply fit with polynomials such that when added to the Rayleigh model for specular reflection, the complete BSDF is reconstructed. Figure 24 shows the fitted data at an illumination angle of  $70^\circ$  for maple leaves. The transmission data is fit with a second order polynomial, while a fourth order polynomial is used for the diffuse reflection. A higher order polynomial is needed for diffuse reflection because the structure of the distribution becomes somewhat more complex at higher incident angles. When the specular reflection component is then added to the corresponding polynomials modeling diffuse reflection, the complete BRDF is reconstructed, as shown for maple leaves in Figure 25.

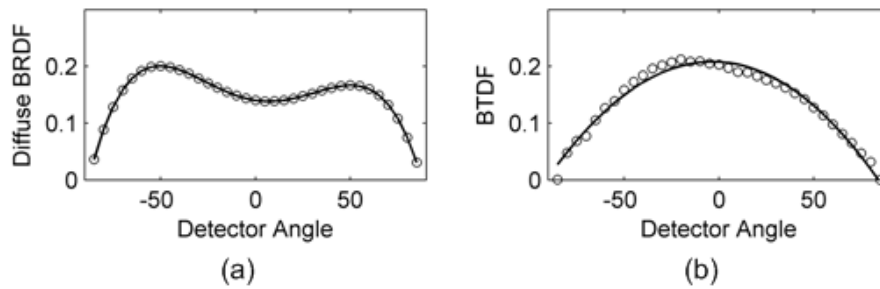


**Figure 24 Fitted Sugar Maple Leaf BSDF Curves for Illumination at  $70^\circ$**

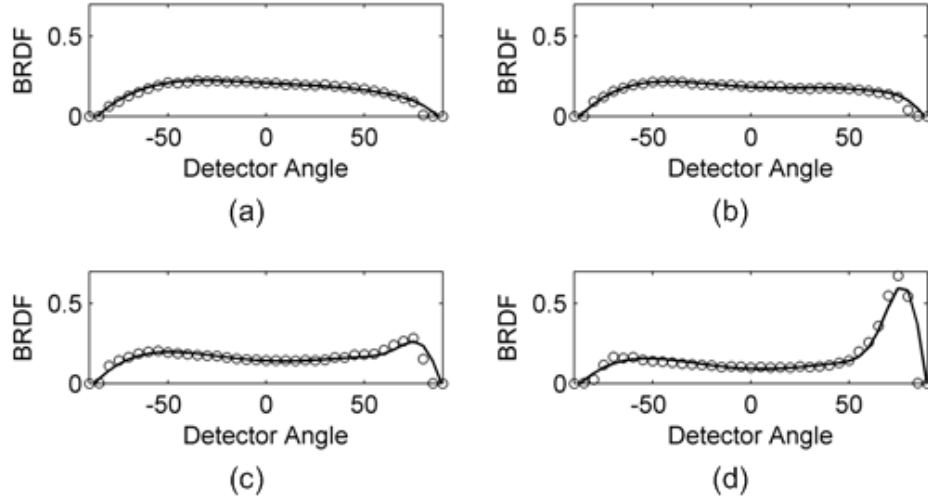


**Figure 25 Sugar Maple Leaf BRDF Models Created by Adding the Diffuse and Specular Components at (a) 50°, (b) 60°, (c) 70°, and (d) 78° Illumination.**

#### 4.1.4. Leaf Data Interpolation

The ability to accurately estimate the BSDF for any illumination angle will be a valuable resource. Thus far, it has been shown that scattering data at the measured illumination angles can be reconstructed using simple polynomial fits and, for high illumination angle BRDF's, a reversed Rayleigh distribution. However, filling in the gaps for intermediate illumination angles requires creating an additional fit to the modeled data. As discussed in the previous two sections, for a given incidence angle, the polynomial equations used to describe the BTDF and diffuse BRDF as a function of both detector  $\theta_D$  and illumination  $\theta_I$  angles are given, respectively, by:

$$t(\theta_D, \theta_I) = p_{1t}\theta_D^2 + p_{2t}\theta_D + p_{3t} \quad (32)$$

$$r_d(\theta_D, \theta_I) = p_{1r}\theta_D^4 + p_{2r}\theta_D^3 + p_{3r}\theta_D^2 + p_{4r}\theta_D + p_{5r} \quad (33)$$

where the polynomial coefficients,  $p$ , are dependent on the illumination angle. With knowledge of these coefficients, the BTDF and diffuse BRDF data can be interpolated at intermediate detector angles for a previously examined illumination angle. However, in order to interpolate BTDF and diffuse BRDF data at intermediate illumination angles it is necessary to examine the relationship between  $\theta_I$  and the value of each of the  $p$ -coefficients. Fitting  $p$  as a function of  $\theta_I$  will allow the interpolation of  $p$  at intermediate illumination angles.

In Figure 26, the  $p$ -coefficients of the maple leaf BTDF data are shown fit with a fourth order polynomial. In general, the fourth order polynomial fits to the  $p$ -coefficients for both BTDF and diffuse BRDF data is defined by a set of five  $q$ -coefficients according to



$$p_{ix}(\theta_i) = q_1\theta_i^4 + q_2\theta_i^3 + q_3\theta_i^2 + q_4\theta_i + q_5 \quad (34)$$

where, for transmission,  $i = 1, 2, 3$  and  $x = t$ , and for reflection,  $i = 1, 2, 3, 4, 5$  and  $x = r$ . Knowledge of the q-coefficient values then allows one to calculate the p-coefficients for any illumination angle through Eqs. (2.12) and (2.13). The q-coefficients calculated for the transmission and diffuse reflection Sugar Maple leaf data are shown in Table 3 and Table 4, respectively. Similarly, values for the Eastern Cottonwood q-coefficients are provided in Table 5 and Table 6.

Using this method of data interpolation we have examined the BSDF estimates at each of the angle permutations used during the data acquisition procedure. The RMS errors found between the originally measured data and the estimates generated through this interpolation method were found to be approximately 2.5% and 1.0% for the BRDF and BTDF of Sugar Maple leaves, respectively. The corresponding RMS errors calculated for Eastern Cottonwood leaves were approximately 3.7% and 1.2%.

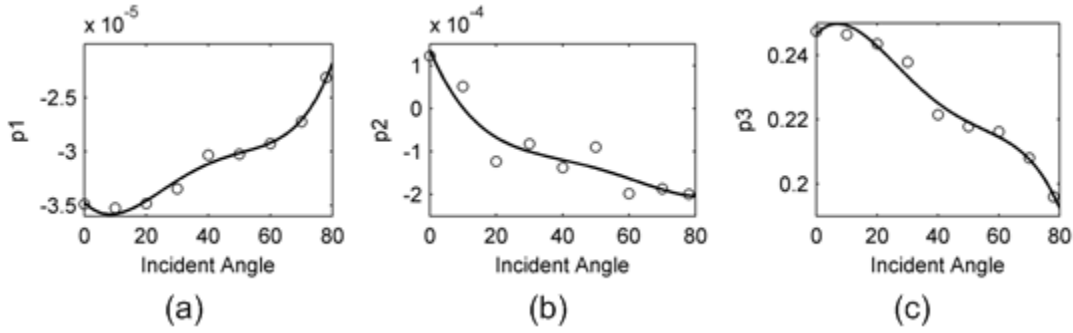


**Figure 26 Polynomial Fits of the (a) 0<sup>th</sup>, (b) 1<sup>st</sup>, and (c) 2<sup>nd</sup> Order p-Coefficients Describing the BTDF Data for Sugar Maple Leaves.**

**Table 3 Sugar Maple leaf BTDF q-Coefficients**

	$q_{1t}$	$q_{2t}$	$q_{3t}$	$q_{4t}$	$q_{5t}$
$p_{1t}$	3.0388e-12	-463.75e-12	23.428e-09	-300.83e-09	-3.4701e-06
$p_{2t}$	34.837e-12	-7.1221e-09	517.86e-09	-17.93e-06	135.77e-06
$p_{3t}$	-10.371e-09	1.6844e-06	-89.529e-06	1.0167e-03	246.48e-03

**Table 4 Sugar Maple leaf BRDF q-Coefficients**

	$q_{1r}$	$q_{2r}$	$q_{3r}$	$q_{4r}$	$q_{5r}$
$p_{1r}$	1.2954e-15	-180.66e-15	6.8481e-12	-132.35e-12	120.16e-12
$p_{2r}$	25.825e-15	-5.0125e-12	285.57e-12	-3.6431e-09	32.217e-09
$p_{3r}$	-10.817e-12	1.5674e-09	-58.687e-09	1.0776e-06	-34.531e-06
$p_{4r}$	-123.8e-12	23.992e-09	-1.2636e-06	8.0717e-06	-164.4e-06
$p_{5r}$	-6.2703e-09	369.59e-09	-12.501e-06	-257.65e-06	245.19e-03

**Table 5 Eastern Cottonwood leaf BTDF q-Coefficients**

	$q_{1t}$	$q_{2t}$	$q_{3t}$	$q_{4t}$	$q_{5t}$
$p_{1t}$	2.5913e-12	-391.07e-12	17.815e-09	-191.88e-09	-34.326e-06
$p_{2t}$	4.4203e-12	-4.1417e-09	325.17e-09	-4.7745e-06	-168.86e-06
$p_{3t}$	-9.2296e-09	1.499e-06	-75.217e-06	738.91e-06	245.53e-03

**Table 6 Eastern Cottonwood leaf BRDF q-Coefficients**

	$q_{1r}$	$q_{2r}$	$q_{3r}$	$q_{4r}$	$q_{5r}$
$p_{1r}$	2.1389e-15	-272.67e-15	8.6857e-12	-111.72e-12	1.6618e-09
$p_{2r}$	-59.223e-15	7.1463e-12	-208.54e-12	1.3098e-09	37.969e-09
$p_{3r}$	-18.62e-12	2.5167e-09	-85.345e-09	1.098e-06	-47.705e-06
$p_{4r}$	479.27e-12	-62.848e-09	2.2671e-06	-23.813e-06	-355.59e-06
$p_{5r}$	5.4467e-09	-1.4462e-06	62.194e-06	-993.25e-06	261.58e-03

#### 4.1.5. Procedure for Constructing the BSDF

BSDF values at any set of angles  $(\theta_l, \theta_d)$  can be accurately estimated for both maple and cottonwood leaves from the information provided herein. Using the following procedure, surface fits for both the BRDF and BTDF can be interpolated for illumination angles spanning a range from  $0^\circ$  to  $78^\circ$ . These are plotted for maple leaves, for example, in Figure 27 and Figure 28, respectively.

- 1) Using Eqs. (26) or (27), calculate the absorption coefficient,  $A_L(\theta_l)$
- 2) Using Eqs. (32) and (34), calculate the BTDF,  $t(\theta_d, \theta_l)$ . The coefficients required for these equations are found in Table 3 and Table 5 for maple and cottonwood leaves, respectively.
- 3) Using Eqs. (33) and (34), calculate the diffuse BRDF,  $r_d(\theta_d, \theta_l)$ . The coefficients required for these equations are found in Table 4 and Table 6 for maple and cottonwood leaves, respectively.
- 4) Generate the specular BRDF,  $r_s(\theta_d, \theta_l)$ , using Eq. (28). Normalize the function to the fractional specular reflection calculated from either Eq. (30) or (31) for maple and cottonwood leaves, respectively.
- 5) Construct the complete BRDF by adding together the specular and diffuse components. That is,

$$r_L(\theta_d, \theta_l) = r_d(\theta_d, \theta_l) + r_s(\theta_d, \theta_l) \quad (35)$$

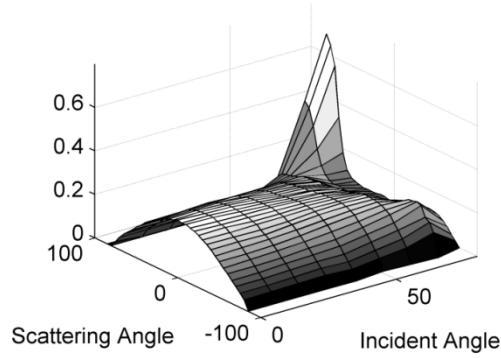


**Figure 27 Two Dimensional BRDF Surface Fit for Sugar Maple Leaves.**

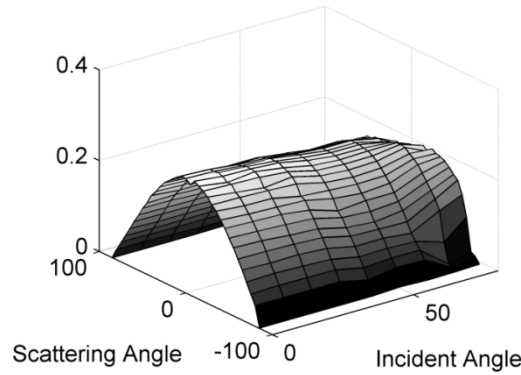


**Figure 28 Two Dimensional BTDF Surface Fit for Sugar Maple Leaves**

Note that the BRDF and BTDF have been normalized in such a way that the sum of their areas plus the absorption coefficient calculated in step (1) is equal to unity. That is,

$$1 = \int_{-90}^{90} i(\theta_D, \theta_I) d\theta_D + \int_{90}^{270} r_L(\theta_D, \theta_I) d\theta_D + A_L(\theta_I) \quad (36)$$

The above steps present a stand-alone method for generating the BSDF of maple and cottonwood leaves for any illumination angle. This method is appropriate for use in remote sensing models where probability density functions describing the scattering by individual leaves must be considered (e.g., in Monte Carlo simulations). Such models typically require examination of the scattering PDFs in both the zenith and azimuth angles. While our models have been developed based only upon in-plane measurements, they may be extended to allow out of plane estimates by assuming azimuthal symmetry in both the diffuse BRDF and the BTDF. We address the asymmetry of the specular component by forcing the azimuth angle to be equal to the angle of incidence in the case of specular reflection. We furthermore believe our models to be largely independent of polarization, though this will require further investigation to verify.

#### ***4.2 Monte Carlo Simulation Results***

Once the canopy parameters from the test forest were incorporated into our model we ran the Monte Carlo simulation and collected spatial, temporal, and angular data in both the ground and receiver planes. Over the period of several weeks, we simulated the launching of ten billion photons into the canopy at an

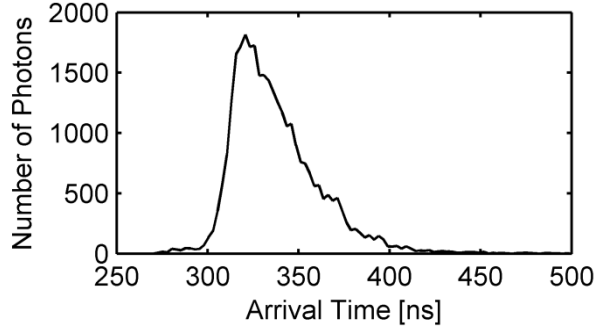


**Figure 29 Characteristic Temporal Waveform from those Simulated Photons which Strike the Canopy Floor**

illumination angle of  $80^\circ$ . This ensured that a sufficient number of photons returned back to the detector plane, allowing us to create smooth probability density functions. Data for all photons that struck the ground plane were considered for the ground plane analysis, while only those photons which returned to the detector, whether they hit the ground or not, were considered in the receiver plane data analysis.

We first divided the virtual ground plane into a grid of  $100 \times 100$  rectangular bins (i.e., the range and cross-range bin dimensions were 3.58m and 2.28m, respectively) and created temporal waveforms, such as the one shown in Figure 30, from the simulated photons arriving within a  $45^\circ$  field of view. This field of view was selected to match that of the detector used in our experiment, as we will discuss later in this section. These waveforms are generally characterized by a sharp peak due to first surface scattered photons, followed by a slowly decaying tail due to the arrival of multiply scattered photons. We then calculated the root mean square (RMS) pulse width of each waveform and also calculated the integrated number of photons falling within each bin. The photons-per-bin values were then normalized with respect to the area of each bin lying within the virtual canopy's elliptical footprint.

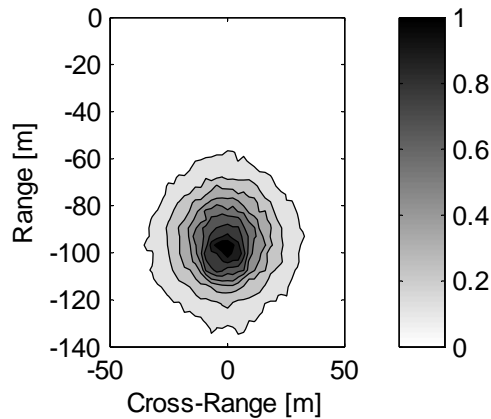


**Figure 30 Simulated Ground Plane Beam Footprint for an Illumination Angle of  $80^\circ$**

A contour plot of the integrated and normalized number of photons arriving within each bin (i.e., the simulated scattered beam footprint), is shown in Figure 31. For clarity this figure has been scaled to a peak value of unity and cropped to highlight the region of greatest interest. Note that all photons are initially propagating in the positive range (x) direction and are aimed at the primary target located at the coordinate system origin at the top of the figure. The center of the large spot on the ground is then positioned beneath the location where photons first enter the canopy (i.e., at  $(x,y) = (-96.66,0)$ ). Recall that the majority of leaves, facing nominally upwards, will be distributed near the top of the canopy. Therefore most photons are scattered downwards just after entering the canopy, which in turn causes the dominant beam footprint to be found beneath the entrance location. This suggests that in practice it might be prudent to illuminate the canopy directly above an anticipated target, rather than at an oblique angle. We then integrated the beam footprint data across both the range and cross-range dimensions, individually, and calculated a best fit Gaussian curve to describe the results. Figure 32 contains the data (dots) and the best fit Gaussian curves (solid) for both the range (a) and cross-range (b) dimensions. The

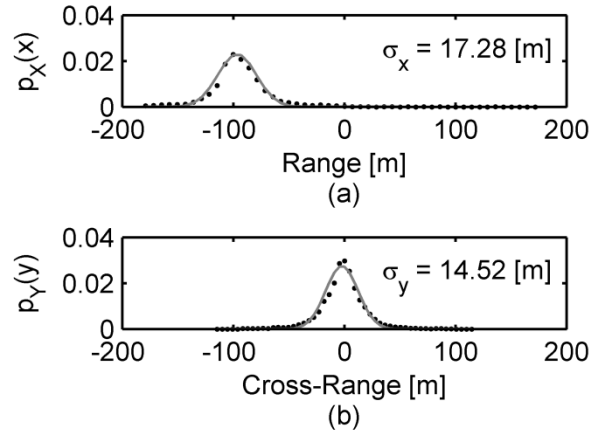


**Figure 31 Simulated Beam Footprint Cross Sections, and Best Fit Gaussian Distributions, in the Range (a) and Cross-Range (b) Dimensions**

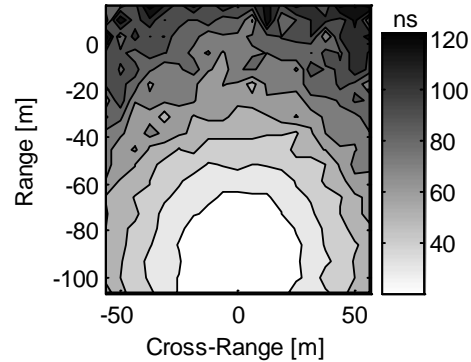


**Figure 32 Spatial Distribution of Simulated RMS Pulse Widths on the Virtual Canopy Floor (in ns)**

standard deviations of the best fit curves (i.e., the RMS ground spot dimensions) were found to be 17.28m for the range dimension and 14.52m for the cross-range dimensions, with RMS fitting errors of  $9.1\text{e-}5$  and  $2.0\text{e-}4$ , respectively.

Next, we created a contour plot of the RMS temporal pulse width (i.e., temporal dispersion) as a function of spatial location as shown in Figure 33, where the gray scale legend has units of nanoseconds. Variations in path length lead to a broad spectrum of transit times through the canopy. Therefore waveforms measured near the canopy entrance location have smaller pulse widths than do those measured further away. Notice, for example, in Figure 33, that the dispersion has a minimum directly beneath the entrance location and increases as the distance from this spot increases.

Additionally, we examined the temporal data for photons incident upon a 25cm diameter virtual detector pupil located in the receiver plane. The 1-D arrival time probability density function for all photons hitting the pupil is shown in Figure 34. The initial sharp rise in the first peak is due to the influx of photons backscattered from high within the canopy, while the slowly decaying tail results from multiply scattered photons. Photons which first hit the secondary target under the canopy entrance location also arrive within the initial peak, but are inseparable from the canopy backscatter noise. Additionally, there is a narrow, sharp peak found near an arrival time of 1.7 microseconds that corresponds to those photons which propagate to and from the primary target without scattering by leaves. These “ballistic” photons are scattered from the primary target back toward receiver pupil with very little deviation (i.e., a very nearly retro reflection). The temporal delay between the initial peak and the unscattered peak exists because photons which propagate to the primary target and back travel a much greater round trip distance than do those which are down-scattered after entering the canopy.

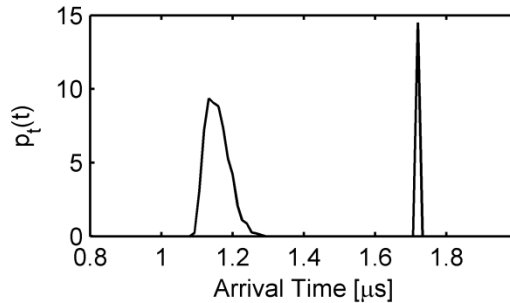


**Figure 33 Simulated 1-D Temporal PDF Measured in Pupil Plane of the Virtual Detector**

### ***4.3 Experimental Verification Results***

A sample mean waveform captured near the entrance location of the canopy is shown in Figure 36. There are two large, narrow spikes at the front edge of the pulse, which we attribute to the direct reflection from some unidentified scatterer, followed by a slowly decaying tail as was seen in the pulse, Figure 36 generated in our simulation. In general, these captured waveforms have more structure than the simulated waveforms, presumably due to the clumping and clustering of leaves and branches. However, the general shape of the measured waveforms is consistent with that of the simulation.



**Figure 34 Image of the Avalanche Photo-Diode Setup**

The normalized beam footprint, created from the integrated energy contained within each waveform, is shown in Figure 37. Note that all photons are initially propagating in the positive direction along the range (x) axis and are aimed at the primary target located at the coordinate system origin. As predicted by the simulation, there is a spot on the ground centered near the entrance location (i.e., at  $(x,y) = (-76,0)$ ) due to the large amount of down scattering just after photons enter the canopy. It appears that there was a slight misalignment between the path we cleared and the beam trajectory, however, as the spot on the ground is seen to be sloping off a bit to the right side in the plot. We attribute this to our cleared path being skewed slightly with respect to the actual beam trajectory. Additionally, there appears to be a small discrepancy in our illumination angle, as we expected the entrance location to be approximately 96.6m in front of the target. At the primary target range we are considering, however, this corresponds to an illumination angle error of only  $1.10^\circ$ .

We then integrated the beam footprint data across both the range and cross-range dimensions, individually, and calculated a best fit Gaussian curve to describe the results. Figure 38 contains the data (dots) and the best fit Gaussian curves (solid lines) for both the range (a) and cross-range (b) dimensions. The standard deviations of the best fit curves were found to be 12.31 m for the range dimension and 8.79 m for the cross-range dimension, with RMS errors of  $1.16e-4$  and  $5.01e-3$ , respectively. To a first order this data matches the predicted beam footprint, shown in Figure 31, in both shape and size, with discrepancies likely due to the fact that our simulated data represents an average over billions of canopy realizations, whereas our experimental data arises from only one actual canopy realization.

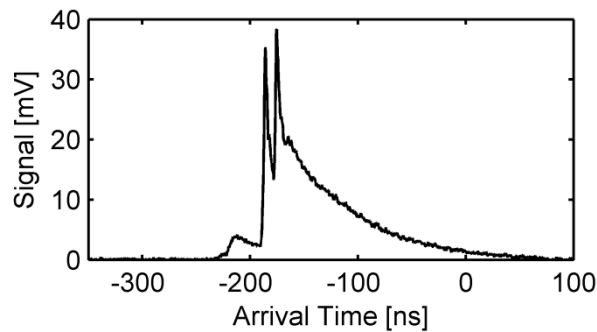


**Figure 35 Characteristic Temporal Waveform Measured by an Upwards Looking Avalanche Photodiode Placed on the Canopy Floor**

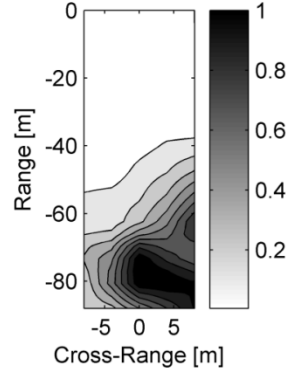


**Figure 36 Measured Ground Plane Beam Footprint for an Illumination Angle of 80°**

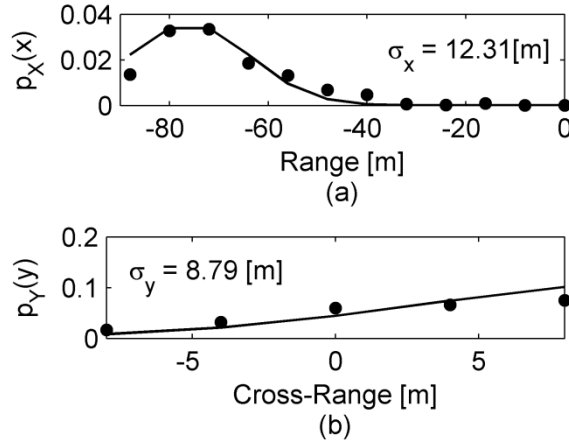


**Figure 37 Measured Beam Footprint Cross-Section Data, and Best Fit Gaussian Curves, in the Range (a) and Cross-Range (b) Dimensions**

Next, the temporal dispersion, or RMS pulse widths of the detected signals, is shown in Figure 39. where the grayscale legend has units of nanoseconds. As predicted by our simulation, the measured dispersion has a minimum directly beneath the entrance location and increases as the radial distance from this spot increases. The misalignment between our cleared the path and the beam trajectory can also be seen in this figure. Once again, discrepancies between our simulated and experimental dispersion are likely due to the fact that our simulated data represents an average over billions of canopy realizations, whereas our experimental data arises from only one actual canopy realization.

Finally, from the tower we collected a series of 511 range gated images of the entire illuminated stand of trees using a gate width of 2ns and a gate delay sequence ranging from 1.20 $\mu$ s to 1.99 $\mu$ s. For each frame, we set a lower threshold to reject detector noise and an upper threshold to eliminate any high intensity first surface reflections. Then, by integrating the pixel values within each thresholded frame, we created a one dimensional probability density function for the photon transit time through the canopy. This is shown in Figure 40. The shape of this plot is very similar to that of the simulated PDF, shown in Figure 33. Both are characterized by an initial peak due to the high density of leaves near the top of the canopy,



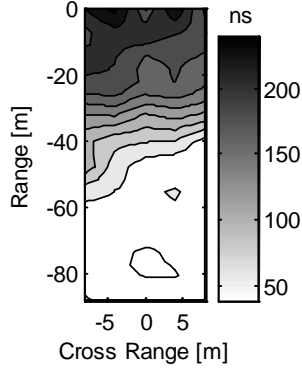


**Figure 38 Spatial Distribution of Actual RMS Pulse Widths Measured on the Canopy Floor**

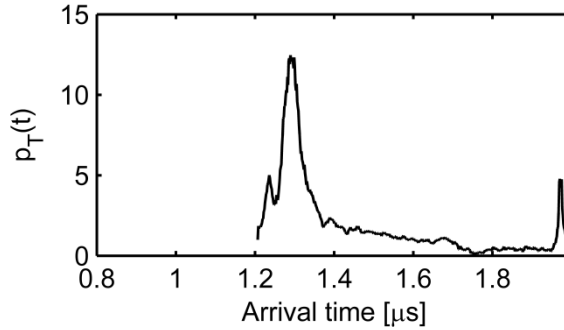


**Figure 39 Actual 1-D Temporal PDF Measured with a Range Gated Intensified CCD Camera Located in the Tower**

each with a width of approximately 100ns. Following the initial peak is a period of very low return, as the few photons that pass through the top of the canopy experience mostly free space propagation until they reach the target. Finally, there is a sharp peak around  $1.75\mu\text{s}$  corresponding to the return of ballistic photons which strike the target and are retro-reflected back towards the receiver.

#### ***4.4 Monte Carlo Results at Various Illumination Angles***

Using this previous work as a basis for model accuracy, we ran our Monte Carlo simulation for illumination angles of  $0^\circ$ ,  $10^\circ$ ,  $20^\circ$ ,  $30^\circ$ ,  $60^\circ$ , and  $80^\circ$  and collected the spatial, temporal and angular data in the ground plane from every launched photon. We then divided the virtual ground plane into a grid of  $100 \times 100$  rectangular bins and created a two-dimensional histogram of the number of simulated photons arriving in each bin within a  $45^\circ$  half field of view. This field of view was selected to match that of the detector used in our experiment described later in this section. The photons-per-bin values were then normalized with respect to the area of each bin lying within the virtual canopy's elliptical footprint.

A contour plot of the integrated and normalized number of photons arriving within each bin (i.e., the simulated scattered beam footprint) is shown in Figure 41 for illumination angles of  $0^\circ$  (a),  $30^\circ$  (b),  $60^\circ$  (c) and  $80^\circ$  (d). For convenience each figure has been scaled to a peak value of unity and cropped to highlight

the region of greatest interest. Note that all photons are initially propagating in the positive range (x) direction and are aimed at the line-of-sight target located at the coordinate system origin at the top of each figure. The center of the large spot on the ground is then positioned approximately beneath the location where photons first enter the canopy for each illumination angle. The actual photon entrance locations, as determined by the illumination angle geometry, and the simulated spot centers are provided in

Table 7. Recall, in our model the majority of the leaves, facing nominally upwards, will be distributed near the top of the canopy. This in turn causes the dominant beam footprint to be found beneath the entrance location. This suggests that in practice it might be prudent to illuminate the canopy directly above an anticipated target, rather than at an oblique angle.

We then integrated the simulated beam footprint data across both the range and cross-range dimensions, individually, and calculated best fit Gaussian curves to describe the results. Figure 42 shows the data (dots) and the best fit Gaussian curves (solid) in both the range (a) and cross-range (b) dimensions for the 80° data. The standard deviations of the best fit curves (i.e., the RMS ground spot dimensions) as well as the RMS fitting errors for each illumination angle are then provided in

Table 8.

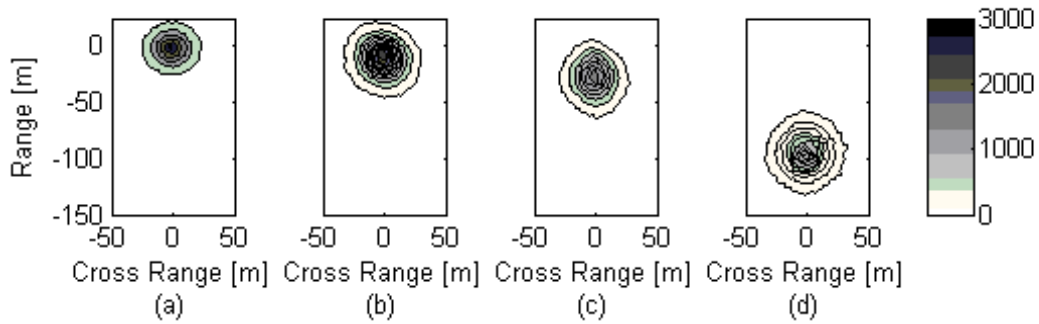


**Figure 40 Simulated Beam Footprint on the Ground for 0° (a), 30° (b), 60° (c) and 80° (d) Canopy Illumination Angles**

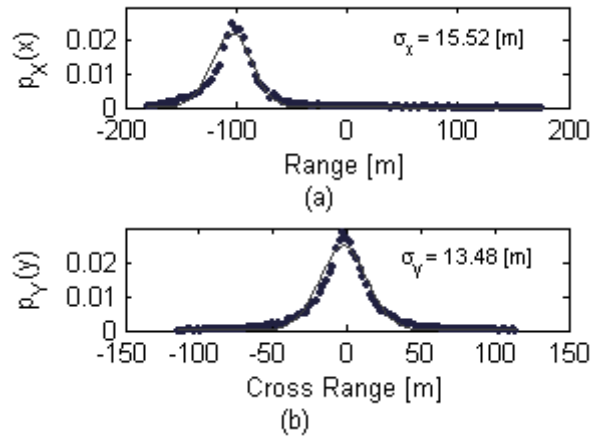


**Figure 41 Cross Section of the Simulated Beam Footprint and Best Fit Gaussian Distribution in the Range (a) and Cross- Range (b) Dimensions**

**Table 7 Actual Photon Entrance Locations and Simulated Principle Spot Centers**

<b>Illum. Angle (deg)</b>	<b>Range Entrance Location (m)</b>	<b>Range Spot Center (m)</b>
0	0	0.0333
10	-3.174	-3.644
20	-6.551	-7.112
30	-10.392	-10.80
60	-31.177	-27.72
80	-102.08	-96.66

**Table 8 Best Fit Gaussian Beam Widths and RMS Fitting Errors**

<b>Illum. Angle (deg)</b>	<b>Range Std (m)</b>	<b>Range Abs Err</b>	<b>Cross Range Std (m)</b>	<b>Cross Range Abs Err</b>
0	13.04	1.608e-4	12.96	1.846e-4
30	14.08	1.892e-4	13.04	1.690e-4
60	14.76	6.366e-5	13.80	1.409e-4
80	15.52	1.253e-4	13.48	2.037e-4

Additionally, we created one-dimensional arrival time probability density functions from photons incident upon a 25cm virtual detector pupil located in the receiver plane, as shown in Figure 43 for canopy illumination angles of 10° (a) and 30° (b). We define signal photons (gray line) to be those which strike the target positioned beneath the entrance location and noise photons (black line) as those which backscatter from the canopy without target interaction. Here we are ignoring the photons returning from the line-of-sight target. As shown previously in this section, illuminating the canopy directly above an anticipated target projects the most energy onto the primary target. Had we known this prior to running our extensive simulation we may not have included a target in line with the initial beam trajectory. Also, especially at higher illumination angles, photons that hit the LOS target and return to the detector plane are almost all ballistic photons; that is, photons that propagate through the gaps between the leaves to and from the LOS target. These ballistic photons represent a very small fraction of photons returned to the detector overall.

In practice we can use a range gated ladar system, which will allow us to open and close the shutter on the camera at very specific time intervals. The time between creating the pulse and opening the shutter on the camera is referred to as the gate delay, and the length of time the shutter remains open is known as the gate width. By using a gate delay approximately equal to the earliest arrival time of the signal photons we may, for example, ignore the initial noise peak, thereby increasing the signal-to-noise ratio. Also, adjusting the gate width will allow us to further increase the SNR.

Moreover, multiple leaf interactions not only lead to temporal delays, but also to spatial and angular dispersion. The volume scattered noise photons are typically more spatially dispersed in the canopy than

are signal photons and therefore generally return to the pupil from more distant locations and often at larger angles. Thus, we are able to further mitigate noise by only accepting photons which are incident upon our detector within a limited field of view. A scatter plot of the arrival time versus arrival angle for photons incident upon the detector is shown in Figure 44. for  $10^\circ$  (a) and  $30^\circ$  (b) canopy illumination angles. Notice that many of the noise photons (black dots) arrive before any of the signal photons (gray dots) and those that arrive at the same time generally come from higher up in the canopy and therefore have a greater angle of arrival.

We consequently investigated the optimization of the signal-to-noise ratio by creating two three-dimensional data matrices containing the number of signal and noise photons arriving within bins of varying gate delay, gate width, and half field of view. The gate delays spanned the range from  $0.2\mu\text{s}$  to  $1.0\mu\text{s}$  with bin spacings of  $0.01\mu\text{s}$ , the gate widths spanned a range from  $0\mu\text{s}$  to  $0.3\mu\text{s}$  with bin spacing of  $0.01\mu\text{s}$ , and the half fields of view spanned a range from  $0^\circ$  to  $40^\circ$  in  $2^\circ$  increments. However, rather than calculating the pre-detection optical signal-to-noise ratio, found by dividing the number of signal photons in each bin by the number of noise photons, we performed a more in-depth analysis by considering several sources of post-detection electrical noise.

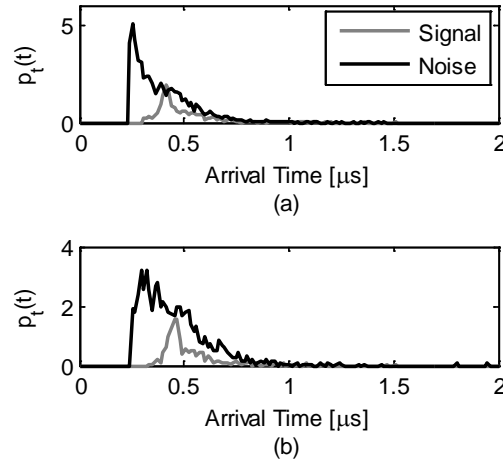


**Figure 42 Photon Arrival Time PDF's without Range Gating or Field of View Filtering for  $10^\circ$  (a) and  $30^\circ$  (b) Canopy Illumination**

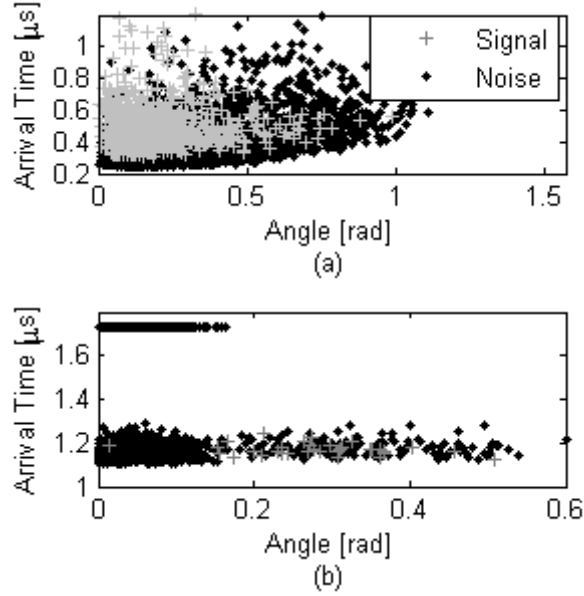


**Figure 43 Scatter Plot of Photon Arrival Time versus Angle of Arrival onto Detector for 10° (a) and 30° (b)**

#### 4.4.1. SNR Calculations

In addition to the backscattered photons, there are several sources of noise which are inherent to the detection process, including shot noise, thermal noise, and dark current noise. The thermal and dark current noises are function of the detector, and are constant in terms of the number of detected photons. Shot noise, however, relies heavily upon the number of photons collected by the detector.

The post-detection electrical SNR can be calculated from these noise sources according to the equation,

$$\text{SNR} = \frac{\langle i_{\text{signal}}^2 \rangle}{\langle i_{\text{dark currents}}^2 \rangle + \langle i_{\text{shot}}^2 \rangle + \langle i_{\text{background}}^2 \rangle + \langle i_{\text{thermal}}^2 \rangle} \quad (37)$$

This equation can be rewritten in terms of the power of the detected photons and detector responsivity,  $R$ , according to the following relation,

$$\text{SNR} = \frac{R^2 \langle P_s^2(t) \rangle}{\left( 2qB(I_D + R \langle P_t(t) \rangle) + R^2 \langle P_n^2(t) \rangle + \frac{4k_B T B}{R_L} \right)} \quad (38)$$

where  $P_s(t)$  is the instantaneous optical signal power,  $P_n(t)$  is the instantaneous background optical noise power, and  $P_t(t)$  is the instantaneous total optical power (i.e., noise + signal) [9,10]. Also note that  $k_B$  is Boltzmann's constant,  $T$  is the temperature (measured in Kelvin),  $B$  is the detector bandwidth (measured in Hz),  $R_L$  is the load resistance,  $I_D$  is the dark current and  $q$  is the charge of an electron.

For a given gate delay and half field of view the instantaneous optical signal power can be calculated from the number of signal photons,  $N_s$ , arriving within the range gate according to the equation,

$$P_s(t) = \frac{h\nu}{\Delta t} N_s(t) \quad (39)$$

The mean-squared optical signal power can be found by integrating this expression over the duration of the range gate,

$$\langle P_s^2(t) \rangle = \frac{1}{T_{gw}} \int_{t_0}^{t_0 + T_{gw}} P_s^2(t) dt \quad (40)$$

where  $t_0$  is the gate delay and  $T_{gw}$  is the gate width. We can approximate this value by breaking the range gate into  $M$  temporal bins and summing the number of signal photons,  $N_{s,i}$ , arriving within each time bin according to the equation,

$$\langle P_s^2(t) \rangle \approx \frac{1}{T_{gw}} \sum_{i=1}^M \left( \frac{h\nu N_{s,i}}{\Delta t} \right)^2 \Delta t \quad (41)$$

After simplification, the mean-squared optical signal power can be expressed as,

$$\langle P_s^2(t) \rangle \approx \frac{(h\nu)^2}{T_{gw} \Delta t} \sum_{i=1}^M N_{s,i}^2 \quad (42)$$

Finally, by applying the relation  $\Delta t = T_{gw} / M$  and the scaling parameter  $\alpha$ , the mean-squared optical signal power can be expressed as,

$$\langle P_s^2(t) \rangle \approx \left( \frac{h\nu}{T_{gw}} \right)^2 M \sum_{i=1}^M (\alpha N_{s,i})^2 \quad (43)$$

where  $T_{gw}$  is the gate width,  $h$  is Planck's constant, and  $\nu$  is the optical frequency. The total number of simulated photons launched into the canopy does not remotely approach the number of photons contained in a single 100mJ pulse from a 1064nm laser, which contains about  $5.4 \times 10^{17}$  photons per pulse. In order to get meaningful results we needed to use signal and noise photon values that would be on the order of what we would expect for a typical laser pulse. Therefore, we scaled the number of signal and noise photons we collected in our simulation by a factor  $\alpha$ , the ratio of the typical number of photons per pulse to the total number of photons we have sent into the canopy. The scaling parameters we used in this calculation are found in Table 12. Note that  $\alpha$  varies with illumination angle as we only simulated enough photons into the canopy to achieve smooth probability density functions, and because a larger percentage of launched photons returned to the virtual detector at lower illumination angles than at larger angles.

Similarly, the mean-squared optical background power can be found from the number of background noise photons,  $N_{n,i}$ , arriving instantaneously within each time bin,

$$\langle P_n^2(t) \rangle \approx \left( \frac{h\nu}{T_{gw}} \right)^2 M \sum_{i=1}^M (\alpha N_{n,i})^2 \quad (44)$$

Finally, the mean total power can be expressed as the sum of the signal and optical background power according to

$$\langle P_t(t) \rangle \approx \frac{h\nu}{T_{gw}} \alpha (N_s + N_n) \quad (45)$$

where  $N_s$  and  $N_n$  are the total number of signal and noise photons, respectively, integrated over all time bins.

#### 4.4.2. Results of Field of View and Range Gate Filtering

Consider, now, that we measure the return of photons in the receiver plane with a PIN photodiode which has the following parameters at a wavelength of 1064nm:  $I_D = 1\text{nA}$ ,  $R = 100\text{mA/W}$  and  $R_L = 1000\Omega$ . Let us also assume a bandwidth of  $B = 2500\text{Hz}$  and a temperature of  $T = 300\text{K}$ . Then, by applying these parameters to Eq. (38) and using the number of signal and noise photons from each bin in our 3-D data matrices, we can construct another three-dimensional data matrix containing the signal-to-noise ratio for each HFOV/gate width/gate delay. We can then use values from this matrix to select the optimal gate delay, gate width and half field of view for achieving the best SNR.

A contour plot of the SNR as a function of both half field of view and gate delay for a constant gate width of  $0.1\mu\text{s}$  is shown in Figure 45 for  $10^\circ$  (a) and  $30^\circ$  (b) canopy illumination angles. The shape of these contour plots is characteristic of the SNR as a function of half field of view and gate delay for most gate widths. In general, the signal-to-noise ratio decreases as the half field of view increases, as mostly noise photons are returning at larger angles. Additionally, the SNR rises, peaks, then decays as the gate delay increases, following the temporal PDF of returning signal photons seen in Figure 45. More importantly, there is a small pocket near a gate delay of  $0.4\mu\text{s}$  where the signal-to-noise ratio is relatively large. Selecting parameters from within this region allows us to achieve a large boost in SNR. Note the location of this high-SNR region shifts to larger gate delays as we increase the illumination angle of photons into the canopy due to the extra optical path distance added by moving the detector further from the target.

**Table 9 Signal-to-Noise Ratios, Gate Delays and Widths, and Half Fields of View for Various Canopy Illumination Angles**

Illumination Angle (deg)	Scaling Parameter	SNR before filtering (dB)	Gate Delay ( $\mu$ s)	Gate Width ( $\mu$ s)	Half field of View (deg)	SNR after filtering (dB)
0	5.65e9	-11.39	0.36	0.02	10	8.88
10	3.15e9	-11.79	0.39	0.06	8	6.61
20	1.51e9	-11.74	0.42	0.10	12	2.52
30	4.02e8	-12.98	0.43	0.04	6	-0.55
60	1.23e8	-20.77	0.54	0.06	8	-0.90
80	3.04e7	-29.57	1.44	0.10	10	-15.20

We located the optimum signal-to-noise ratio from well-populated bins within this pocket. It is important to note that optimum does not necessarily mean maximum, as there are several bins that are populated by only a few photons. The SNR values for these bins were specific to the exact realization of our simulation and not representative of the actual signal-to-noise ratio. We therefore disregarded angular/temporal bins with fewer than 50 returning photons.

We found that using a  $0.39\mu$ s gate delay, a  $0.06\mu$ s gate width and an  $8^\circ$  half field of view produced optimal signal-to-noise ratio improvement in the  $10^\circ$  illumination angle data, while a  $0.43\mu$ s gate delay,  $0.04\mu$ s gate width, and a  $6^\circ$  half field of view optimally enhanced the SNR of the  $30^\circ$  data. We calculated that applying these filters increased the signal-to-noise ratio of the  $10^\circ$  and  $30^\circ$  data from -11.39dB to 8.88dB and -12.98dB to -0.55dB, respectively. Figure 46 displays the one-dimensional arrival time probability density functions previously seen in Figure 43 after both range gating and field of view filtering have been applied. Note that the signal is now larger than the noise for the  $10^\circ$  data and on the same order as the noise for the  $30^\circ$  data. The calculated SNR values, optimum range gates and half field of view filters for several other illumination angles are found in Table 9 with generally the same order of increase in SNR.

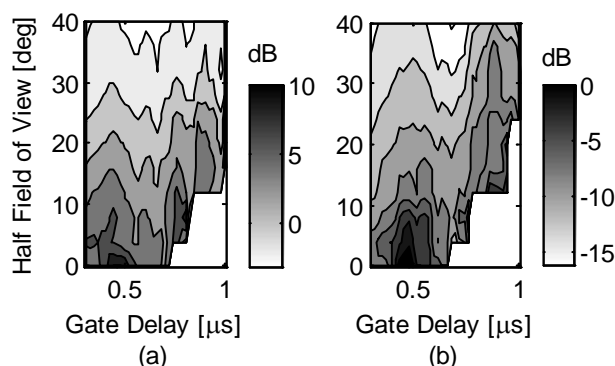


**Figure 44 Contour Plot of SNR as a Function of Gate Delay and Half Field of View after Field of View for a Gate Width of  $0.1\mu$ s for  $10^\circ$  (a) and  $30^\circ$  (b) Canopy Illumination**



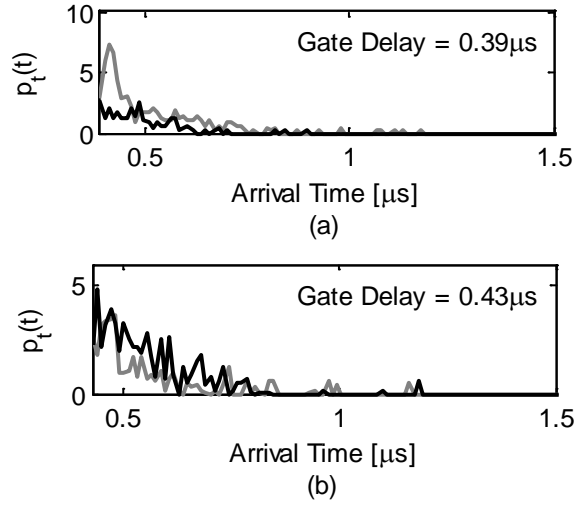


**Figure 45 Photon Arrival Time PDF's after both Range Gate and Field of View Filtering for 10° (a) and 30° (b) Canopy Illumination**

#### 4.4.3. Additional SNR Considerations

While we included the total average photon count due to background as a noise term in the denominator in Eq. (38), there are several instances, for example thermal imaging, in which only the shot noise due to the background is included in the denominator.

$$\text{SNR} = \frac{R^2 \langle P_s^2(t) \rangle}{\left( 2qB(I_D + R \langle P_t(t) \rangle) + \frac{4k_B TB}{R_L} \right)} \quad (46)$$

To illustrate the effect of only keeping the background shot noise contribution, we recalculate Table 9 to show the SNR for the case that the total average photon count due to background is removed from the denominator. This is shown in Table 10.

**Table 10 Signal-to-Noise Ratios, Gate Delays and Widths, and Half Fields of View for Various Canopy Illumination Angles**

Illum. Angle (deg)	Scaling Parameter	SNR before Filtering (dB)	Gate Delay (μs)	Gate Width (μs)	Half field Of View (deg)	SNR after filtering (dB)
0	5.65e9	-11.39	0.36	0.02	10	15.95
10	3.15e9	-11.79	0.39	0.06	8	13.23
20	1.51e9	-11.74	0.42	0.10	12	7.61
30	4.02e8	-12.98	0.43	0.04	6	3.47
60	1.23e8	-20.77	0.54	0.06	8	-0.89
80	3.04e7	-29.57	1.44	0.10	10	-9.46

## 5. Conclusions and Recommendations

We have presented a Monte Carlo model used to simulate the propagation and scattering of light through a dense tree canopy. The model is characterized by the probability density functions governing several parameters, such as the leaf number density, the angular orientation of leaves, and the bidirectional scattering distribution functions of individual leaves. We then measured the physical dimensions and the leaf area density of a nearby grove of trees, as well as the angle and distance between our tower and the target location within this tree grove. We then applied these values to the model.

We ran our simulation for  $80^\circ$  illumination and examined the expected beam footprint and pulse width profile on the ground, as well as the temporal returns we would expect to measure at the receiver. Then, in order to validate the model, we illuminated our tree grove with a 780 nm beam. We measured waveforms on the canopy floor with a  $5 \times 12$  grid of upwards facing avalanche photodiodes and collected range gated images using an ICCD camera located in the tower.

As predicted by the simulation, we experimentally verified that a large number of photons are down scattered just after entering the canopy, creating a large spot on the ground beneath the entrance location. We then found that a Gaussian distribution fit the range and cross-range cross-sections of the simulated and measured beam footprints with great accuracy. We also found that the standard deviations of the best-fit Gaussian distributions were on the same order in both simulation and experiment. Additionally, we observed that the pulse widths of the waveforms measured on the ground were similar in both shape and magnitude to those predicted by our simulation. Finally, we found that the measured 1-D temporal PDF of photons returning to the receiver closely matched the PDF predicted by the simulation.

We believe that any mismatch between our simulation and experimental results can be attributed to two factors. First, in the experiment there was a slight misalignment between the trajectory of the initial beam axis and the path cleared in the tree grove, which resulted in a small angular error in the pointing of our beam. Second, and most importantly, the simulation results represent an average over billions of realizations of the canopy while the experiment considers only one real forest realization. Considering these factors, we believe our experimental results correlate very well with our simulation, leading us to conclude that our model is valid.

We then investigated the ability of the canopy propagation model to handle seasonal canopy variations. We first quantified the effects of seasonal changes on two forest parameters: the bidirectional scattering distribution function of individual leaves and the maximum leaf area density of the canopy. Then by applying these parameters to our Monte Carlo canopy propagation model we predicted the effect of seasonal changes on the shape and size of the beam footprint as measured on the ground. We found that as the forest health declines and the leaves fall from the trees the size of the spot on the ground increases. We then experimentally verified the results of the model by illuminating a real forest with a 780nm beam and sampling the beam footprint with an upwards facing APD beneath the canopy. The same trend was seen in the experimentally measured data as was predicted by the simulation.

Finally, we used our Monte Carlo canopy propagation model to make predictions about detecting objects through the canopy at several different illumination angles. We have used our Monte Carlo propagation model to simulate the scattering of photons through a dense canopy using several different illumination angles. We found that the scattered beam footprint on the canopy floor is primarily located beneath the entrance location of photons into the canopy for all illumination angles. As a result, illuminating the canopy above an anticipated target, rather than aiming directly at it, places more photons on the target and immensely increases the signal-to-noise ratio of detectable returning photons.

Additionally, we examined the effects of using a narrow field of view, range gated camera. We found that multiply-scattered photons spend more time in the canopy than do singly-scattered photons, and therefore generally arrive at the virtual receiver plane at a later time. The use of a range gated camera allows us to look past the initial return of backscattered noise photons, increasing the signal-to-noise ratio. Multiple canopy scattering also causes spatial and angular dispersion of photons throughout the canopy. Thus, photons arriving at later times most likely also arrive at larger angles, which allows many noise photons to be filtered using a narrow field of view camera.

We found that by illuminating directly above the desired target and using a narrow field of view, range gated camera we found that we can boost the signal-to-noise ratio on the order of 15dB. While our results are specific to the exact geometry and canopy architecture used in this simulation, we have demonstrated in principle that we may boost the signal-to-noise ratio of detected multiply scattered photons using a narrow field of view, range gated camera, ultimately providing the possibility of imaging obscured targets embedded within a dense forest canopy at low illumination angles.

## 6. References

- <sup>1</sup> H. Guo, D. Liang, Y. Wang and X. Huang, "Detection of invisible moving targets in foliage penetration ultra-wide-band synthetic aperture radar images," *Opt. Eng.* **42**, 2796-2804 (2003)
- <sup>2</sup> M. Soumekh, "Moving target detection in foliage using along track monopulse synthetic aperture radar," *IEEE Trans. Image Process.* **16**, 1148-1163 (1997)
- <sup>3</sup> M. Soumekh, "Reconnaissance with ultra-wide-band UHF/VHF synthetic aperture radar," *IEEE Signal Process. Mag.* **12**, 20-40 (1995)
- <sup>4</sup> M. W. Roth, J. C. Hunnell, K. E. Murphy and A. E. Scheck, "High-resolution foliage penetration with gimbaled lidar," in *Laser Radar Technology and Applications XII*, G. W. Kamerman, ed., (SPIE, 2007)
- <sup>5</sup> R. M. Marino and W. R. Davis Jr., "Jigsaw: a foliage-penetrating 3D imaging laser radar system," *Lincoln Laboratory Journal*, **15**, 23-36 (2005)
- <sup>6</sup> B. W. Schilling, D. N. Barrm, G. C. Templeton, L. J. Mizerka and C. W. Trussell, "Multiple-return laser radar for three-dimensional imaging through obscurations," *Applied Optics* **41**, 2781-2799 (2002)
- <sup>7</sup> J. T. Murray, S. E. Moran, N. Roddier, R. Vercillo, R. Bridges, and W. Austin, "Advanced 3D polarimetric flash ladar imaging through foliage," in *Laser Radar Technology and Applications VIII*, G. W. Kamerman, ed., (SPIE, 2003), pp. 84-95
- <sup>8</sup> J. Liu, R. A. Melloh, C. E. Woodcock, R. E. Davis and E. S. ochs, "The effect of viewing geometry and topography on gap fractions through forest canopies," *Hydrological Processes* **18**, 3595-3607 (2004)
- <sup>9</sup> F. T. Ulaby, K. C. McDonald, K. Sarabandi, M. Whitt, and M. C. Dobson, "Michigan Microwave Canopy Scattering Model (MIMICS)," *Proc. IGARSS '88* (Edinburgh, UK) p1009 (1988)
- <sup>10</sup> R. B. Myneni, J. Ross, and G. Asrar, "A review of the theory of photon transport in leaf canopies," *Agriculture and Forest Metrology*, **45**, 1-153 (1989)
- <sup>11</sup> S. Jaquemoud, S. L. Ustin, J. Verdebout, G. Schmuck, G. Andreoli, and B. Hosgood, "Estimating leaf biochemistry using the PROSPECT leaf optical properties model," *Remote Sensing of Environment*, **56**, 194-202 (1996)
- <sup>12</sup> S. Jaquemoud and F. Baret, "PROSPECT: a model of leaf optical properties spectra," *Remote Sensing of Environment*, **34**, 75-91 (1990)
- <sup>13</sup> S. Jaquemoud and S. Ustin, "Leaf Optical Properties: A state of the art," *Proc. 8<sup>th</sup> International Symposium Physical Measurements & Signatures in Remote Sensing*, Aussois (France), CNES, 223-232 (2001)
- <sup>14</sup> Lt P. Muller, L. Barnes, and M. Dierking, "See through leaves," *Combat ID Technology Branch AFRL/SNJM*
- <sup>15</sup> H. T. Breece III and R. A. Holmes, "Bidirectional Scattering Characteristics of Healthy Green Soybean and Corn Leaves in Vivo," *Appl. Opt.* **10**, 119-127 (1971)
- <sup>16</sup> T. T. Lei, R. Tabuchi, and T. Koike, "Functional relationship between chlorophyll content and leaf reflectance, and light-capturing efficiency of Japanese forest species," *Physiol. Plant* **96**, 411-418 (1996)
- <sup>17</sup> J. Ross and T. Nilson, "A mathematical model of radiation regime of plant cover (in Russian)," *Actinometry and Atmospheric Optics*, 263-281 (1968)
- <sup>18</sup> J. K. Shultis and R. B. Myneni, "radiative transfer in vegetation canopies with anisotropic scattering," *J. Quant. Spectrosc. Radiat. Transfer* **39**, 115-129 (1988)
- <sup>19</sup> T. W. Brakke, "Goniometric measurements of light scattered in the principle plane from leaves," *Geoscience and Remote Sensing Symposium* **2**, 508-510 (1992)
- <sup>20</sup> J. T. Woolley, "Reflectance and transmittance of light by leaves," *Plant Physiol.* **47**, 656-662 (1971)
- <sup>21</sup> B. W. Schilling, D. N. Barrm, G. C. Templeton, L. J. Mizerka and C. W. Trussell, "Multiple-return laser radar for three-dimensional imaging through obscurations," *Applied Optics* **41**, 2781-2799 (2002)
- <sup>22</sup> J. T. Murray, S. E. Moran, N. Roddier, R. Vercillo, R. Bridges, and W. Austin, "Advanced 3D polarimetric flash ladar imaging through foliage," in *Laser Radar Technology and Applications VIII*, G. W. Kamerman, ed., (SPIE, 2003), pp. 84-95
- <sup>23</sup> J. Lui, R. A. Melloh, C. E. Woodcock, R. E. Davis and E. S. ochs, "The effect of viewing geometry and topography on gap fractions through forest canopies," *Hydrological Processes* **18**, 3595-3607 (2004)
- <sup>24</sup> T. W. Brakke, "Specular and diffuse components of radiation scattered by leaves," *Agr. For. Meteorol.* **71** 283-295 (1994)
- <sup>25</sup> E. A. Bucher, "Computer simulation of light pulse propagation for communication through thick clouds," *Applied Optics* **12**, 2391-2400 (1973)
- <sup>26</sup> C. Kittel and H. Kroemer, *Thermal Physics*, W.H. Freeman, San Francisco (1980)

- <sup>27</sup> K. C. McDonald, M. C. Dobson, and F. T. Ulaby, "Using MIMICS to model L-band multiangle and multitemporal backscatter from a walnut orchards," *IEEE Transactions on Geoscience and Remote Sensing* **28**, 477-491 (1990)
- <sup>28</sup> R.B. Myneni, J. Ross, and G. Asrar, "A review of the theory of photon transport in leaf canopies," *Agriculture and Forest Metrology*, **45**, 1-153 (1989)
- <sup>29</sup> M.A. Karam and A.K. Fung, "A canopy scattering model and its application to a deciduous forest," *IEEE*, 137-140 (2000)
- <sup>30</sup> D.S. Falster and M. Westoby, "Leaf size and angle vary widely across species: what consequences for light interception?," *New Phytologist*, **158**, 509-525 (2003)
- <sup>31</sup> M. Abramowitz and I. A. Stegun, "Laplace Transforms" in *Handbook of Mathematical Functions with Formulas, Graphs and Mathematical Tables*, (New York: Dover, 1972), pp. 1020-1021
- <sup>32</sup> E.F. Gilman and D.G. Watson, "Acer saccharum sugar maple", Fact Sheet ST-51 Environmental Horticultural Department, Florida Cooperative Extension Service, Institute of Food and Agricultural Sciences (1993)
- <sup>33</sup> J. Ross, V. Ross, and A. Koppel, "Estimation of leaf area nad its vertical distribution during growth period," *Agricultural and Forest Meteorology* **101**, 237-246 (2000)
- <sup>34</sup> B. Lalic and D.T. Mihailovic, "An empirical relation describing leaf-area density inside the forest for environmental modeling," *American Meteorological Society* **43**, 641-645 (2004)
- <sup>35</sup> T. Brakke, "Goniometric measurements of light scattered in the principle plane from leaves," *IEEE Geoscience and Remote Sensing*, 508-510 (1992)
- <sup>36</sup> J. L. Privette, R. B. Myneni, W. J. Emery, and B. Pinty, "Inversion of a soil bidirectional reflectance model for use with vegetation refelectance models," *Journal of Geophysical Research* **100**, 479-508 (1995)
- <sup>37</sup> S.F. Ray, "The fisheye lens and immersed optics," in *Applied Photographic Optics*, (Focal Press, 2002), pp.327-332

## Appendix A: Calculation of Probability of a Ballistic Photon

In this appendix we derive the expression for calculating the probability of encountering an unscattered photon in the Monte Carlo simulation. Before proceeding directly into the derivation for calculating the probability of an unscattered photon, it is important to note a fundamental statistical rule concerning conditional probability. Assume that A and B denote two events and  $P(A|B)$  denotes the conditional probability of A occurring given that B has already occurred. Baye's Theorem then gives the relationship between the two stochastic events to be,

$$P(A|B) = P(B|A) \frac{P(A)}{P(B)}. \quad (\text{A.1})$$

Recall, in the simulation we have broken the inhomogeneous canopy into 50 horizontal slices of constant leaf number density. We did this so that the probability density function governing the random propagation distance within each region could be modeled as a negative exponential, expressed as,

$$p_d(d) = \frac{1}{D} \exp\left[-\frac{d}{D}\right], \quad (\text{A.2})$$

where,  $D$  is the mean free path, which is a function of leaf number density.

The probability that a photon *will* interact with a leaf within a region  $[d_1, d_2]$  of constant leaf number density, illustrated in Figure 61, is the integral of the PDF over that region,

$$P\{d_1 < d < d_2\} = \int_{d_1}^{d_2} p_d(d) dd. \quad (\text{A.3})$$

Then the probability that the photon *will not* interact with a leaf in the region  $[d_1, d_2]$  is equal to one minus the probability that there will be an interaction,

$$P\{\overline{d_1 < d < d_2}\} = 1 - \int_{d_1}^{d_2} p_d(d) dd. \quad (\text{A.4})$$

Because of the segmented canopy, the calculation of the probability of an unscattered photon must be done one region at a time. So, the probability of not having an interaction in the  $i^{\text{th}}$  region is dependent upon the probabilities of there being an interaction in any of the previous regions. This is best explained by making the first few iterations of the method.

To begin, let the mean free path of the  $i^{\text{th}}$  region to be denoted  $D_i$  and the boundaries of the  $i^{\text{th}}$  region to be  $[d_{i-1}, d_i]$ . Then, the probability that there will not be an interaction in the first region is given by the expression,

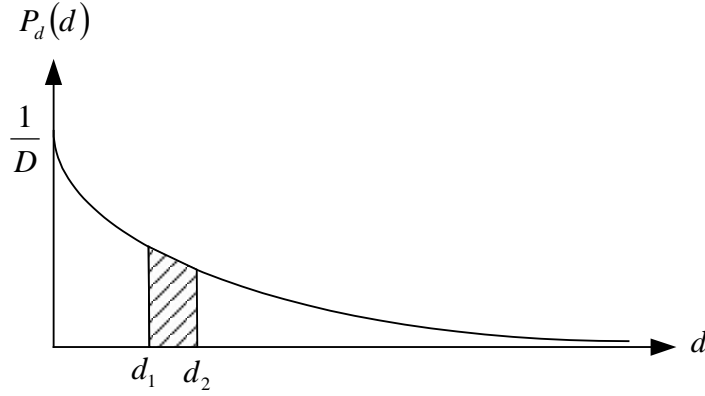


**Figure A-1 Probability that a Photon will Interact with a Leaf within the Region  $d_1$  to  $d_2$  is Given by the Integral of the Negative Exponential PDF over that region**

$$P\{0 \leq d \leq d_1\} = \frac{\int_0^{d_1} \frac{1}{D_1} \exp\left[-\frac{d}{D_1}\right] dd}{\int_0^{\infty} \frac{1}{D_1} \exp\left[-\frac{d}{D_1}\right] dd} \quad (\text{A.5})$$

As has already been expressed, the probability of there *not* being an interaction in the first region is then given by one minus this value,

$$P\{\overline{0 \leq d \leq d_1}\} = 1 - \frac{\int_0^{d_1} \frac{1}{D_1} \exp\left[-\frac{d}{D_1}\right] dd}{\int_0^{\infty} \frac{1}{D_1} \exp\left[-\frac{d}{D_1}\right] dd} \quad (\text{A.6})$$

The probability of interaction in the second region is conditional, given that the photon has already propagated out of the first region. That is, let A denote the event “photon propagated through region 1 without interaction,” and let B denote the event “interaction occurs in region 2.” Then Baye’s Theorem says that the probability that the photon will have an interaction in region 2, given that it has already propagated through region 1 is given by,

$$P(B|A) = P(A|B) \frac{P(B)}{P(A)} \quad (\text{A.7})$$

We can read the first term  $P(A|B)$  on the right side of the expression to be, “the probability of the photon propagating through region 1, given that an interaction occurs in region 2.” If the interaction occurs in region 2, then the photon *must have* propagated through region 1 without interaction. Therefore, this value is always unity and Eq. (B.7) can be rewritten,

$$P(B|A) = \frac{P(B)}{P(A)} \quad (\text{A.8})$$

To evaluate this expression, consider Figure A-2. The probability that an interaction occurs in region 2 is the integral of the PDF over the boundaries of region 2,

$$P\{B\} = P\{d_1 < d < d_2\} = \int_{d_1}^{d_2} \frac{1}{D_2} \exp\left[-\frac{d}{D_2}\right] dd \quad (\text{A.9})$$

This region is illustrated by the area marked with negatively sloped lines. The probability that the photon propagated to region 2 without interaction is denoted by the area marked with the positive sloped lines and given by the integral of the PDF from the beginning of region 2 to the extent of the range,

$$P\{A\} = P\{d_1 \leq d\} = 1 - \int_0^{d_1} \frac{1}{D_2} \exp\left[-\frac{d}{D_2}\right] dd = \int_{d_1}^{\infty} \frac{1}{D_2} \exp\left[-\frac{d}{D_2}\right] dd \quad (\text{A.10})$$

Then, the probability that there will be an interaction in region 2, given that the photon has propagated through region 1 is found by substituting equations (A.9) and (A.10) into expression (A.8). Subtracting this from unity gives the probability of there not being an interaction in region 2, given that there was no interaction in region 1.

$$P(\overline{B}|A) = 1 - \frac{\int_{d_1}^{d_2} \frac{1}{D_2} \exp\left[-\frac{d}{D_2}\right] dd}{\int_{d_1}^{\infty} \frac{1}{D_2} \exp\left[-\frac{d}{D_2}\right] dd} \quad (\text{A.11})$$

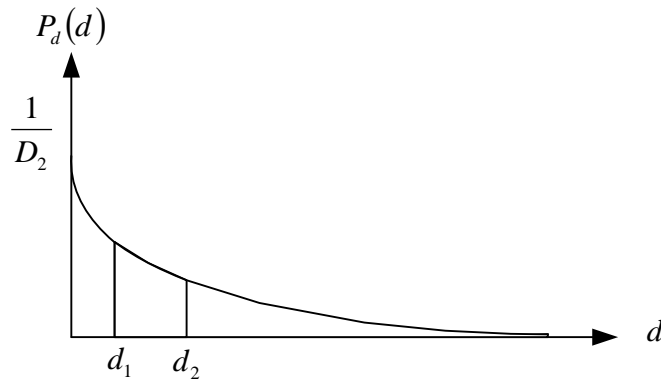


**Figure A-2 The Probability Density Function that a Photon will have an Interaction**



Finally, one can extend this computational stencil to the  $i^{\text{th}}$  region.

$$P\left(\overline{d_{i-1} \leq d \leq d_i} \middle| d_{i-1} \leq d\right) = 1 - \frac{\int_{d_{i-1}}^{d_i} \frac{1}{D_i} \exp\left[-\frac{d}{D_i}\right] dd}{\int_{d_{i-1}}^{\infty} \frac{1}{D_i} \exp\left[-\frac{d}{D_i}\right] dd} \quad (\text{A.12})$$

And the total probability that there will not be any interaction throughout the entire canopy will be the product of all the probabilities calculated for each region,

$$P\left(\overline{0 \leq d \leq h}\right) = \prod_{n=1}^N \left[ 1 - \frac{\int_{d_{n-1}}^{d_n} \frac{1}{D_n} \exp\left[-\frac{d}{D_n}\right] dd}{\int_{d_{n-1}}^{\infty} \frac{1}{D_n} \exp\left[-\frac{d}{D_n}\right] dd} \right] \quad (\text{A.13})$$

## Appendix B: APD Field of View Characterization

Prior to performing the waveform measurement experiments we characterized the field of view of the avalanche photodiode (APD). Initially we had planned to mount a narrow band pass filter on the APD so that we could perform our waveform measurement experiments during the day, however, as the results within this appendix show, the field of view with the band pass filter in place was too narrow.

We made use of the BRDF measurement apparatus previously used to measure the bidirectional scattering distribution functions of leaves, which is depicted in Figure B-1. We directed a linearly polarized (at  $20^\circ$  with respect to vertical), 1064 nanometer pulsed laser ( $>6\mu\text{J}$  pulse energy) along the axis of a stationary optical rail. We then used a polarizer and two wave plates to attenuate the beam to avoid damaging the sensitive APD.

We directed the reflection from the second wave plate towards a 50% reflective Spectralon® disc and detected the pulses with a InGaAs PIN diode. We used the measured radiant energy reflected from this disc as both a trigger to signal measurements from the APD and also as a pulse energy monitor so that data could later be normalized with respect to variations in pulse energy.

We used two neutral density filters, mounted on the rail after the beam splitter to further attenuate the power of the laser in order to avoid damaging the APD. The ND filters were tilted slightly in order to avoid direct reflections into the beam path. Any deflection of the beam due to the first filter was counteracted by the second so that the path of the beam remained along the rail axis.

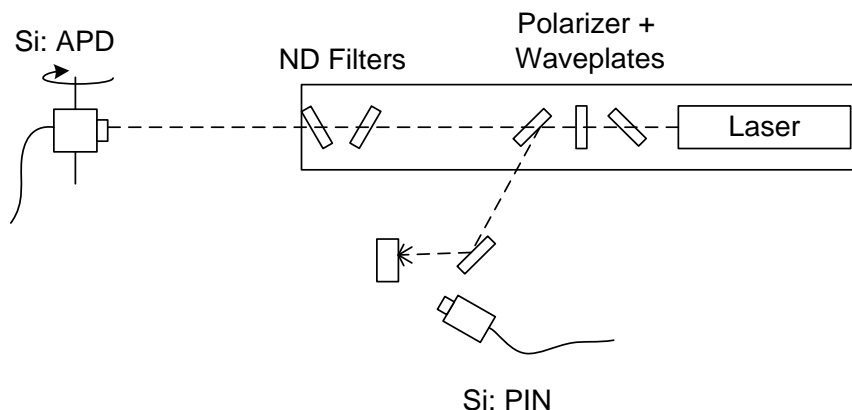


**Figure B-1 Schematic Depiction of the Experimental Setup**

After attenuation, we directed the laser beam onto the Hamamatsu C5658 High Speed APD Module which was mounted on a motor driven and computer controlled rotation stage which also tracked the APD's rotational position relative to the beam path. This rotation stage is capable of  $360^\circ$  of rotation, allowing the APD to be illuminated at any angle.

The motors of both the detector rail and leaf mount were controlled by an automated LabView® program which rotated the detectors and leaf to predetermined angles. At each set of angles the program collected 512 samples from each detector. The samples were then averaged, and a mean value was stored for each detector. The program then moved the leaf and/or detectors to the next set of angles, and the process was repeated until all the desired angle permutations are exhausted.

Alignment of the system was critical. Slight misalignment of the active area of the APD and the axis of rotation of the rotation stage would result in very large errors. We aligned the system by mounting a cap with crosshairs onto the front of the APD such that the crosshairs were centered on the active area. A near-IR camera was also set up so that it was focused onto the crosshairs/active area of the APD. With the laser illuminating the crosshairs, we translated the rotation stage such that the center of the beam fell just above the “X” on the crosshairs, as seen in Figure B-2. Because the crosshairs were mounted out in front of the active area and the camera was mounted above the laser (looking slightly downward), we wanted the beam spot to be slightly higher than the “X” on the crosshairs. This placed the beam directly on the center of the active area.



**Figure B-2 The Beam is Incident on the Crosshairs Just Above the “X”**

We placed a piece of scotch tape on the monitor and drew dot on the center of the beam spot, which can also be seen in Figure B-2 above. Then we turned off the laser and positioned the APD so that the dot on the monitor fell exactly on the center of the active area. Note that only the two transverse directions may be aligned in this fashion. To align the axial component, we rotated the APD to some angle, say  $30^\circ$ , then translated the APD along the axis until the dot on the monitor fell exactly at the center of the active area.



**Figure B-3 Images of the active area of the APD (a) at  $0^\circ$  rotation and (b) at  $40^\circ$  rotation**

Once alignment was finished, we turned off the lights to reduce the ambient light and rotated the polarizer to extinguish as much of the beam as possible. We then placed ND filters with optical densities of 400 and 250 in the beam path to further diminish the signal. Using the computer and the “Interactive Moving Leaves” program (LabView code written by John Schmoll) we rotated the APD to the desired angles and recorded the 512 sample average at each angle.

The field of view data of the APD with the band pass filter in place is found in Table B-1 and the field of view data of the APD by itself is found in Table B-2. The field of view of the detector with the band pass filter in is only on the order of  $10^\circ$ , whereas that of the APD by itself is approximately  $50^\circ$ . This is in accordance with the specifications of the APD module, which affirm that the field of view is approximately  $48^\circ$ .

**Table B-1 Field of view data of the APD with the band pass filter**

<b>Angle (deg)</b>	<b>APD Ch1 Max (mV)</b>	<b>PIN trigger Ch2 Max (mV)</b>
0	231.4	31.98
2	225.3	32.97
4	186.7	32.67
5	115.9	32.54
6	45.61	32.50
8	0	32.62
-2	225.6	32.72
-4	212.9	32.26
-5	201.7	32.01
-6	144.8	31.82
-8	22.20	32.09
-10	0	31.32

**Table B-2 Field of view data of the APD without the band pass filter**

<b>Angle (deg)</b>	<b>APD Ch1 Max (mV)</b>	<b>PIN trigger Ch2 Max (mV)</b>
0	438.9	31.63
5	437.3	31.7
10	415	31.52
15	399.4	31.47
20	370.4	31.28
25	364.3	32.41
30	322	32.26
35	265.2	32.54
40	224.4	31.98
45	184.1	32.12
-5	433.5	31.67
-10	409.6	31.27
-15	384.6	31.59
-20	372.4	31.57
-25	342.5	31.35
-30	317.7	31.99
-35	284.1	30.69
-40	242.8	31.07

The data in the absence of the band pass filter is plotted in the Figure B-4. The drop off of the APD signal as a function of angle is due to several phenomena, the first being the cosine dependence of the projected area. As the APD is rotated to higher angles, less of the active area is projected into the direction of illumination. The angular dependence of the reflection coefficient at dielectric boundaries also adds to the dwindling of the signal as the incidence angle increases. There are two such dielectric interfaces: (1) air/silicon boundary at the active area and (2) air/borosilicate glass boundary at the window. Finally, the curve seen on the figure is the theoretical signal expected when the projected area and reflection coefficients are taken into consideration. The theoretical curve is normalized to the maximum value of the detected signal, which happens to occur at an angle of  $0^\circ$ .

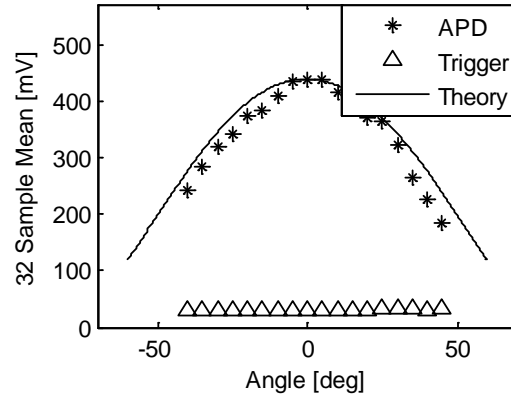


**Figure B-4 Hamamatsu C5658 APD Module Field of View Characterization**

## Appendix C: Test Canopy GPS Waypoints

In Section 3 we discussed measuring the dimensions of the test canopy in order to create the most reproducible results from the simulation. The data and details of the calculation are found in this appendix.

We measured the dimensions of a nearby wooded area using an eTrex Vista™ hand held GPS unit. We periodically stored waypoints around the perimeter of the tree grove and converted the latitude/longitude coordinates into differential distances from a reference location. The logged waypoints (solid dots) and corresponding approximate errors (surrounding circle) for each point are illustrated in Figure C-1. Note that the reference waypoint is marked with blue in the following figure. The data for the locations of these waypoints is located in Table C-1.



**Figure C-1 The Locations of the Waypoints are Overlain onto a Satellite Image**

Conveniently, the tower from which field tests are conducted is directly east of the wooded area. Therefore, we could circumscribe an ellipse around the woods with the major axis equal to the longitudinal distance between two waypoints on the horizontal edge of the canopy. We used waypoints 22 and 14 as the principle locations on the horizontal axis. The two are separated in longitude by a distance of 371 meters. Similarly, the minor axis of the canopy was calculated from the latitudinal distance between two waypoints on the vertical edge of the canopy. We used waypoints 3 and 17 as two chief locations on the vertical axis. The two are separated in latitude by a distance of 229 meters. The ellipse circumscribing the tree stand is shown in Figure C-2.

**Table C-1 Longitudinal/latitudinal locations of waypoints and differential distance from the reference waypoint\*\***

Waypoint	Latitude	Differential Distance (m)	Longitude	Differential Distance (m)
1**	46.674	0	5.1	0
2	46.687	24.01214376	5.137	68.34225533
3	46.714	73.88351927	5.189	164.3908304
4	46.702	51.71846349	5.219	219.8034698
5	46.692	33.24758367	5.257	289.9928131
6	46.686	22.16505578	5.274	321.3933088
7	46.692	33.24758367	5.287	345.4054526
8	46.678	7.388351927	5.294	358.3350685
9	46.706	59.10681542	5.285	341.7112766
10	46.717	79.42478322	5.3	369.4175964
11	46.694	36.94175964	5.322	410.053532
12	46.676	3.694175964	5.325	415.5947959
13	46.66	-25.85923175	5.327	419.2889719
14	46.652	-40.6359356	5.311	389.7355642
15	46.643	-57.25972744	5.289	349.0996286
16	46.631	-79.42478322	5.287	345.4054526
17	46.59	-155.1553905	5.268	310.3107809
18	46.586	-162.5437424	5.206	195.7913261
19	46.588	-158.8495664	5.17	129.2961587
20	46.601	-134.8374227	5.152	96.04857505
21	46.624	-92.35439909	5.109	16.62379184
22	46.647	-49.87137551	5.11	18.47087982



**Figure C-2 The Canopy is Taken to be an Elliptical Cylinder with Minor Axis Length of 115 Meters and Major Axis Length of 185 Meters**

## Appendix D: Cable Delay and Dispersion

In Section 4 we reported on the experimental verification of our Monte Carlo canopy propagation model. In these sections we discussed the methodology we used to measure the waveforms from the canopy floor. Recall that we sent a trigger beam towards a target in the clearing which we detected with a PIN diode. We sent the signal from this detector through a 500ft cable into the forest into the oscilloscope, which was stationed with the rest of our data collection system. We then sent the main beam into the canopy and measured the waveforms on the ground with the APD, which was also connected to the oscilloscope.

The two waveforms collected during the waveform experiment were temporally misaligned due to different cable lengths connecting the detectors to the scope. The objective of this test was to determine the temporal delays so that the waveform data may be synched.

We connected the output of a function generator to channel 1 of an oscilloscope using a cable of arbitrary length and a T-connector. We then connected one end of the 500ft trigger cable to the T-connector and the other end to channel 2 of the scope. We then generated a 100kHz, 8ns pulse with a 10 $\mu$ s period using the function generator and stored the pulses after propagation through the cables. The amplitude of the pure pulse was 1V peak-to-peak and the edge time was 5ns.

The measured pulses using the 500ft trigger cable are shown in Figure D-1, where the baseline pulse has a maximum at 3.6ns and the trigger pulse has a maximum at 795.2ns. The time delay between the pulses is then 791.6ns. Also, the baseline pulse width is 9.4ns and the trigger pulse width is 22.2ns.

The measured pulses using the APD cable are shown in Figure D-2, where the baseline pulse has a maximum at 3.6ns and the ADP pulse has a maximum at 59.2ns. The time delay caused by the APD cable is then 55.6 ns. Also, the APD cable broadened the pulse width from 9.4ns to 9.6ns.



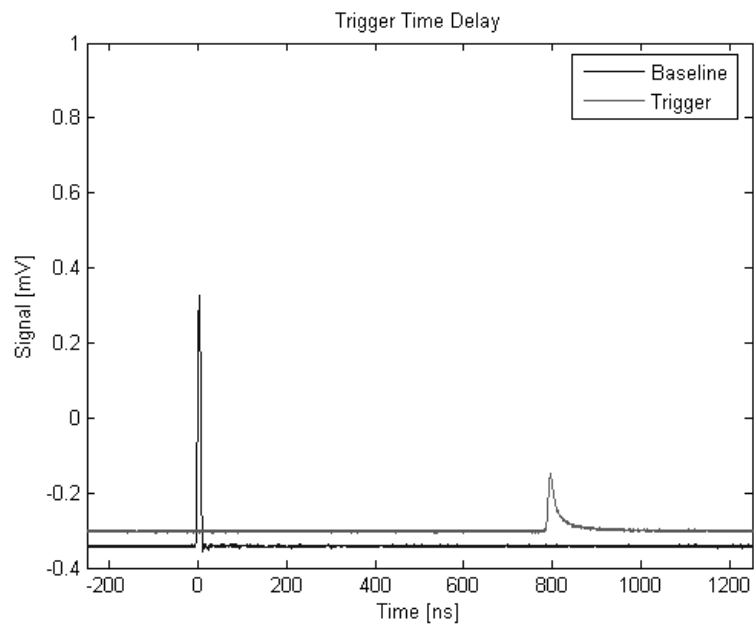


**Figure D-1 Temporal Delay and Dispersion Cause by the Trigger Cable**

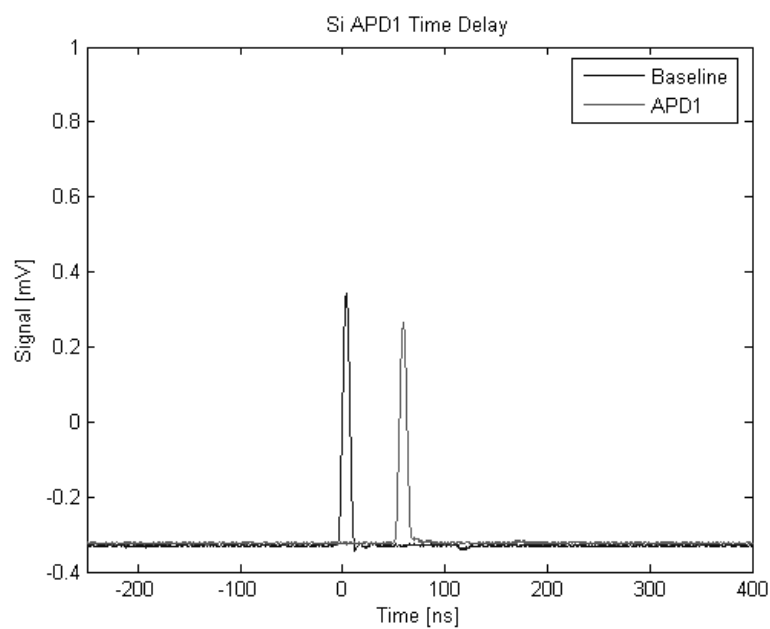


**Figure D-2 Temporal Delay and Dispersion Caused by the APD Cable**

## Appendix E: Selection of Random Value

Nearly all technical computing software has a built-in function to generate uniformly distributed random variables between 0 and 1. Often times, however, we desire to select specific values of a random variable described by a non-uniform probability density function. The procedure for doing so is actually quite simple.

In general, consider a random variable  $Y$  which can be described as a function of another random variable  $X$  (i.e.,  $Y = f(X)$ ). If  $X$  is a random variable uniform on  $[0,1)$ , and if we know the probability density function  $p_Y(y)$  for  $Y$ , then for any given randomly chosen value of  $X$  the corresponding random value selection for  $Y$  is governed by the relationship

$$y = f(x) = F_Y^{-1}(x). \quad (\text{F.1})$$

where  $x$  and  $y$  represent specific values of the random variables  $X$  and  $Y$ , respectively, and where  $F_Y(y)$ , known as the Cumulative Distribution Function (CDF) of  $Y$ , is the indefinite integral of  $f_Y(y)$ .

## List of Acronyms, Abbreviations and Symbols

Acronym	Description
<b>APD</b>	<b>Avalanche Photo-Diode</b>
<b>BRDF</b>	<b>Bi-Directional Reflection Distribution Function</b>
<b>BSDF</b>	<b>Bi-Directional Scattering Distribution Function</b>
<b>BTDF</b>	<b>Bi-Directional Transmission Distribution Function</b>
<b>CDF</b>	<b>Cumulative Distribution Function</b>
<b>IR</b>	<b>Infrared</b>
<b>LAD</b>	<b>Leaf Area Density</b>
<b>ND</b>	<b>Neutral Density</b>
<b>NIR</b>	<b>Near Infrared</b>
<b>PDF</b>	<b>Probability Density Function</b>
<b>RMS</b>	<b>Root-Mean-Square</b>
<b>SAR</b>	<b>Synthetic Aperture Radar</b>
<b>SNR</b>	<b>Signal-to-Noise Ratio</b>
$A$	<b>Absorptance</b>
$T$	<b>Transmittance</b>
$R$	<b>Reflectance</b>
$\theta_D$	<b>Detector Angle</b>
$\theta_I$	<b>Illumination Angle</b>
$\theta_{INC}$	<b>Incidence Angle</b>
$\theta_L$	<b>Leaf Zenith Angle</b>
$\phi_L$	<b>Leaf Azimuth Angle</b>
$\theta_S$	<b>Leaf Scattering Zenith Angle</b>
$\phi_S$	<b>Leaf Scattering Azimuth Angle</b>
$\theta$	<b>Photon Propagation Zenith Angle</b>
$\phi$	<b>Photon Propagation Azimuth Angle</b>
$\theta_T$	<b>Target Scattering Zenith Angle</b>
$\phi_T$	<b>Target Scattering Azimuth Angle</b>
$\theta_G$	<b>Ground Scattering Zenith Angle</b>
$\phi_G$	<b>Ground Scattering Azimuth Angle</b>
$d$	<b>Photon Propagation Distance</b>
$D(z, \theta)$	<b>Mean Free Path</b>
$\overline{A}_p(\theta)$	<b>Mean Projected Area</b>
$N(z)$	<b>Leaf Number Density</b>
$A_p$	<b>Projected Area</b>
$A_0$	<b>Mean Leaf Area</b>
$d_L$	<b>Mean Leaf Diameter</b>

Acronym	Description
$u(x - x_0)$	Unit Step Function
$p_X(x)$	Probability Density Function
$L(z)$	Leaf Area Density
$L_m$	Maximum Leaf Area Density
$h$	Canopy Height
$z_m$	Vertical Canopy Location corresponding to Maximum Leaf Area Density
$R$	Detector Responsivity
$q$	Charge of Electron
$B$	Detector Bandwidth
$T$	Temperature
$R_L$	Load Resistance
$k_B$	Boltzmann's Constant
$I_D$	Dark Current
$N_S(t)$	Number of Signal Photons
$P_S(t)$	Instantaneous Optical Signal Power
$N_N(t)$	Number of Noise Photons
$P_N(t)$	Instantaneous Optical Noise Power
$h$	Plank's Constant
$\nu$	Frequency of Light
$T_{gw}$	Gate Width
$M$	Number of Temporal Bins
$\alpha$	Photon Scaling Parameter
$P_t(t)$	Instantaneous Optical Detected Power